Deriving Tidal Constituent Estimates From GNSS Buoy Data in the Arctic

Vasulkar, A. N.; Verlaan, M.; Slobbe, D. C.

DOI
10.1029/2024EA003775

Publication date
2025

Document Version
Final published version

Published in
Earth and Space Science

Citation (APA)
Vasulkar, A. N., Verlaan, M., & Slobbe, D. C. (2025). Deriving Tidal Constituent Estimates From GNSS Buoy Data in the Arctic. *Earth and Space Science*, *12*(7), Article e2024EA003775. https://doi.org/10.1029/2024EA003775

ADVANCING EARTH AND SPACE SCIENCES

Earth and Space Science

RESEARCH ARTICLE
10.1029/2024EA003775

Deriving Tidal Constituent Estimates From GNSS Buoy Data in the Arctic

A. N. Vasulkar[1,2], **M. Verlaan**[1,2], **and D. C. Slobbe**[3]

[1]Delft Institute of Applied Mathematics, Delft, The Netherlands, [2]Hydrodynamics and Forecasting, Deltares, Delft, The Netherlands, [3]Geosciences and Remote Sensing, Civil Engineering and Geosciences, Delft, The Netherlands

Key Points:

- Tidal current constituents for surface currents can be estimated from single GNSS buoy trajectories with the proposed new method
- In areas with large tidal phase gradients, that is, short wavelengths, tidal frequencies can shift considerably through Doppler shift mechanism
- Tidal phase gradients, not directly derivable from buoy data, can be estimated using tide model-based gradients

Correspondence to:

A. N. Vasulkar,
a.n.vasulkar@tudelft.nl

Citation:

Vasulkar, A. N., Verlaan, M., & Slobbe, D. C. (2025). Deriving tidal constituent estimates from GNSS buoy data in the Arctic. *Earth and Space Science*, *12*, e2024EA003775. https://doi.org/10.1029/2024EA003775

Received 28 MAY 2024
Accepted 15 JUN 2025

Author Contributions:

Conceptualization: A. N. Vasulkar, M. Verlaan
Data curation: A. N. Vasulkar
Formal analysis: A. N. Vasulkar
Funding acquisition: M. Verlaan, D. C. Slobbe
Investigation: A. N. Vasulkar
Methodology: A. N. Vasulkar, M. Verlaan
Project administration: M. Verlaan, D. C. Slobbe
Resources: A. N. Vasulkar
Supervision: M. Verlaan, D. C. Slobbe
Validation: A. N. Vasulkar, M. Verlaan, D. C. Slobbe
Visualization: A. N. Vasulkar
Writing – original draft: A. N. Vasulkar
Writing – review & editing: M. Verlaan, D. C. Slobbe

Abstract

Measurements of tides are relatively sparse in the Arctic. This paper studies GNSS buoy tracks to complement existing data. Existing methods to perform tidal harmonic analysis of the buoy data are inadequate in the Arctic region because these methods for tidal analysis combine data from multiple buoy tracks, which is often infeasible in the Arctic. Moreover, we find that there are significant spatial and temporal variations in amplitudes and phases in baroclinic zones. To address these complexities, we introduce a new approach–Model-derived Fitting Method–to estimate the tidal current constituents (TCC) from a single buoy trajectory. Our study assesses the proposed method by analyzing GNSS buoy data from three Arctic regions characterized by barotropic or baroclinic tidal currents. Through detailed case studies in the Barents Sea, Chukchi Sea, and Baffin Bay, our approach demonstrates accuracy, robustness, and operational capabilities. In the Barents Sea, TCC estimates from two buoys were compared at a common location within their trajectories and compared against model estimates. In the Chukchi Sea's barotropic dominant zone, our method's estimates were evaluated against nearby ADCP mooring data. In Baffin Bay, known for baroclinic currents, a synthetic evaluation confirmed the method's effectiveness. Our study also highlights that phase variations along buoy trajectories can lead to frequency shifts in the spectrum, similar to the Doppler shift effect, particularly notable in regions with baroclinic tides.

Plain Language Summary

In the Arctic, measuring tidal currents and water levels is challenging due to harsh conditions and ice cover. However, recent Arctic expeditions have used GPS-equipped buoys to track ice and water movements, offering new ways to measure currents. Arctic currents are complex, varying across locations and over time, which renders traditional analysis methods ineffective. In this study, we developed a new way to analyze the GPS data from these buoys to figure out the patterns of ocean currents. Our method considers the unique challenges of the Arctic and provides a more accurate picture of how the water moves in different areas, whether it's in regions where currents are relatively uniform or in more complex zones where the currents can change dramatically over short distances. We validated our method using buoy data from three Arctic regions and through a simulated test in a complex current zone. Our results show that this method is effective and offers a better tool for understanding Arctic currents, crucial for marine ecosystem protection, ship navigation, and resource management in this sensitive region.

1. Introduction

Tidal currents play a crucial role in the Arctic, impacting everything from the health of marine ecosystems to the subdaily scale sea ice dynamics (Luneva et al., 2015; Watkins et al., 2023). In addition, precise tidal current information is essential for navigation, fisheries, and resource exploration (Baumann et al., 2020), which are becoming increasingly vital as marine traffic intensifies with the ongoing decline in sea ice (Boylan, 2021).

Arctic tidal models provide insights into tidal currents, but there is limited data regarding the accuracy of their tidal current estimates for example, (Cancet et al., 2018; Erofeeva & Egbert, 2018; Lyard et al., 2021; Müller et al., 2014; Verlaan et al., 2015, among others). Observations from Acoustic Doppler Current Profilers (ADCPs) give tidal current estimates at their mooring locations. The Arctic Tidal Current Atlas (Baumann et al., 2020) offers tidal current estimates based on historical mooring data, but it does not provide real-time information. Another challenge is the significant spatio-temporal variability in tidal current estimates, especially in the strong baroclinic tidal zones of the Arctic such as the Nares Strait (Baumann et al., 2020), which emphasize the need to have well-distributed ADCP network. But the harsh Arctic environment poses challenges for deploying the ADCPs (Munchow et al., 1995), compounded by the need for specialized equipment to prevent ice buildup on the instruments (Nyström, 2022). These issues highlight the need for new or additional data sources.

GNSS buoys that track surface ocean currents present a promising additional data source. Expeditions like the Multidisciplinary drifting Observatory for the Study of Arctic Climate (MOSAiC) (Bliss et al., 2022, among others) have enhanced buoy deployments in the Arctic. Innovations, such as the solar-powered Spotter buoy (Raghukumar et al., 2019) developed by Sofar Technologies, Inc, ensure extended operational periods even in severe Arctic winter conditions (Kodaira et al., 2021). The International Arctic Buoy Programme (IABP) further contributes by offering extensive real-time and historical data (IABP, 2020). Contemporary buoys, boasting high temporal resolution, typically ranging from 15 min to 6 hr, grant detailed insights into the variability of tidal currents.

However, the presence of sea ice in the Arctic presents challenges for using these buoy data. Firstly, buoys cannot be deployed in landfast ice regions. In drifting sea ice regions, buoy trajectories result from air-ice-water interactions and may not accurately represent underlying tidal currents, as sea ice internal stress dampens tidal movements of the buoys (Koentopp et al., 2005). Moreover, the Arctic lies in the critical latitude of the semidiurnal tidal frequency, leading to potential contamination from the inertial frequency (Pease et al., 1983). These can be addressed to some extent by considering buoys only in the free drift regimes of the drifting sea ice. Vasulkar et al. (2022) have shown that under low wind conditions, in a free drift sea ice field the buoys move along with the tides and have the same movement as the underlying tidal currents. This makes it possible that at least part (free drift and open ocean) of the buoy trajectories can be used to estimate tidal surface currents in the Arctic. Consequently, however, doing so limits the availability of "usable" buoy trajectories to estimate tidal current constituents (TCC) in the Arctic.

Other issues in TCC estimation from buoy data are challenges which are not encountered with traditional tidal harmonic analysis used in ADCPs. These buoys traverse both space and time, tracking surface tidal currents. In regions where surface tidal currents align with depth-averaged barotropic currents, buoys effectively track the barotropic flow. However, when these currents traverse rough topographies or steep inclines, a conversion from barotropic to baroclinic tides is observed (Simmons et al., 2004), resulting in surface currents that deviate from depth-averaged tidal flows. The smaller spatial scales of baroclinic tides compared to barotropic tides (Apel, 2003; Simmons et al., 2004) can cause a Doppler shift in the tidal frequencies observed by the buoy, rendering traditional tidal harmonic analysis ineffective. Another challenge is that the changes in stratification can result in changes to the baroclinic tides and as a consequence, TCCs are not constant along the buoy trajectory.

Several methods target TCC estimation from buoy trajectories, with most of them focussing on barotropic tides. Lie et al. (2002) presented two methods for the Yellow and East China Sea. Their *correction method* segments trajectories into semidiurnal and diurnal components. And each of the components is estimated separately to obtain the amplitude and phase for M_2 and K_1 with other components (S_2, N_2, O_1, P_1) derived using constant amplitude ratios and phase differences with respect to these components. These fixed amplitude ratios and phase differences were obtained from observations in the region. Addressing the limitations of this approach, they proposed what is referred to as the *fitting method*. This approach builds on top of the correction method but considers varying amplitudes and phases, fitting them to nth-order polynomials. While adaptable to regions with baroclinic tides, its treatment of Doppler shift remains unclear. Here, selecting the proper order of the polynomial is also challenging without knowing the variations of amplitude and phase. The methods rely on a large number of buoy data, where estimates from multiple buoy trajectories in the region are used to compute an average estimate for the region. Moreover, accounting for the non-linear interaction between tides and the mean current would make the optimization challenging.

Poulain and Centurioni (2015) created a global tidal current data set (excluding poleward regions) from extensive drifter data over 15 years. Their method involved a tidal harmonic analysis of the buoy trajectories using an approach similar to Lie et al. (2002). They sub-divided the buoy trajectories into 15− day periods for eight constituents and averaged estimates over a $2° \times 2°$ grid. These were benchmarked against global ocean tide models, showing good accuracy but with notable standard deviation. A challenge of their method for the Arctic is the reliance on extensive multi-year buoy data, and the assumption of constant TCCs, which may not apply in baroclinic dominant regions. Kodaira et al. (2016) adjusted the constant tidal current assumption of Poulain and Centurioni (2015) in baroclinic zones by using a finer $0.5° \times 0.5°$ grid. Their method multiplies slow-moving polynomial-fitted buoy positions by harmonic terms for the M_2 amplitude and phase. However, in this method, too, the need for large amount of buoy data remains a challenge for the Arctic.

Overall, existing methods are inadequate in addressing the unique challenges presented by the Arctic environment. This inadequacy is evident in the need for accurate TCC estimates from single buoy trajectories, a requirement stemming from the limited availability of buoy data in the Arctic. Additionally, the significant spatio-temporal variability in amplitudes and phases, coupled with the potential frequency shift in buoy trajectory spectra, further emphasize the need for precise and adaptable tidal estimation procedures tailored to Arctic conditions.

In this paper, we introduce a method for conducting tidal harmonic analysis of single buoy trajectories accounting for space-time variations: the *Model-derived Fitting method*. The accuracy and applicability of this method will be validated through case studies involving buoys located in three distinct Arctic regions: the Barents Sea, Chukchi Sea (barotropic zones), and Baffin Bay (baroclinic zone). Furthermore, we demonstrate that the Doppler shift phenomenon can lead to frequency shifts in the angular frequency of tidal harmonics as observed by the buoy. We analyzed the spectrum of two buoy trajectories in regions with both barotropic and baroclinic tidal current dominance in the Arctic. In this analysis, observed frequency shifts are compared with theoretical shifts in the spectrum, focussing on the peak for the M_2 tidal frequency.

In Section 2, we outline the proposed method for tidal analysis on buoy trajectories along with the mathematics of the Doppler shift. Section 3 delineates the data and models utilized in the study. Section 4 shows the results of the Doppler shift experiment with the following section (Section 5) focussing on the three case studies. Finally, Section 6 summarizes the key conclusions of this paper.

2. Tidal Analysis of the Buoys

2.1. Harmonic Analysis–Preliminaries

The GNSS buoys provide trajectory data, which we refer to as *position time series* in this chapter. Using these series, we can calculate velocity time series through a central difference scheme. This velocity series can be decomposed into two components: a low-frequency currents and high-frequency (i.e., tidal) currents:

$$\boldsymbol{u}(x,y,t)=\boldsymbol{u}_m(x,y,t)+\boldsymbol{u}_t(x,y,t), \tag{1}$$

where $\boldsymbol{u}$ represents the velocity vector of the buoy, $\boldsymbol{u}_m$ denotes the low-frequency currents, and $\boldsymbol{u}_t$ represents the high frequency (tidal currents). The functions $y(t)$ and $x(t)$ correspond to the latitude and longitude of the buoy's position at time t. The low-frequency currents can be removed by filtering or polynomial fitting for example, (Kodaira et al., 2016; Lie et al., 2002; Vasulkar et al., 2022, among others). Some authors (e.g., Lie et al., 2002) also include a wind-driven and inertial component. For simplicity, we'll postpone this discussion until later.

The tidal component can be approximated by a tidal harmonic expansion, as shown below:

$$u_t(x,y,t)=\sum_{i\in\{\mathrm{TH}\}}H_i(x,y,t)\cos\big(\omega_i t-\phi_i(x,y,t)\big), \tag{2}$$

where u_t is the meridional component of $\boldsymbol{u}_t$, $\{\mathrm{TH}\}$ denotes the list of tidal harmonics or constituents, and ω_i represents the angular frequency of the i^{th} harmonic with its corresponding amplitude H_i and phase ϕ_i. Similarly, for the zonal component of the velocity (v_t), we have,

$$v_t(x,y,t)=\sum_{i\in\{\mathrm{TH}\}}G_i(x,y,t)\cos(\omega_i t-\theta_i(x,y,t)), \tag{3}$$

where the amplitude (G_i) and the phase (θ_i) correspond to the i^{th} harmonic. For a thorough decomposition of the time series, nodal factors and initial phase considerations are essential. Although, for brevity in this text, we've left out these factors from the discussed expressions. Nonetheless, we have incorporated the nodal factors in our calculation of the tidal harmonics. The magnitude and nature of Arctic tidal currents can be seen in the Arctic tidal current atlas from Baumann et al. (2020) which provides a spatio-temporal distribution of the tidal currents.

2.2. Challenges in Doing a Tidal Analysis

Performing a traditional tidal harmonic analysis on GNSS buoy data presents unique challenges due to the non-stationary nature of the buoys. The key issues are as follows:

2.2.1. Spatio-Temporal Variability in Amplitudes and Phases

The amplitude and phase of the tidal harmonic fitting to the velocity time series of the buoy are functions of both space and time. The amplitude and phase of the TCCs can vary along the trajectory, differing from what would be observed at a fixed point. When this spatio-temporal variability is not taken into account, the movement of the buoy at best leads to an averaging of the amplitude and phase estimates over the trajectory of the buoy. But this averaging can lead to large errors in regions with large spatial variations in amplitudes and phases.

2.2.2. Frequency Shift Due To Phase Variability

Due to the dependence of the phase on space and time, the angular frequency of the tidal harmonics observed by the buoy is affected. In this section, we show this mathematically for the phase of the meridional velocity. Doing a first-order Taylor approximation of the phase $\left(\phi_i(x,y,t)\right)$ in the cosine component of Equation 2, we get:

$$\hat{\phi}_i^n \approx \omega_i t - \phi_i^0 - \frac{\partial \phi_i}{\partial x}\Delta x - \frac{\partial \phi_i}{\partial y}\Delta y, \tag{4}$$

where $\hat{\phi}_i^n$ is the total (net) phase within the brackets of the cosine term, Δx is the average buoy movement in the $x-$ direction and likewise, Δy is the average buoy movement in the $y-$ direction. ϕ_i^0 is the phase at the initial position of the position time series. The subscript (i) denotes that this is for the i^{th} TCC. $\phi_i(x,y,t)$ being a function of time alters the frequency ω_i. To see this, consider the average velocity of the buoy given by:

$$\overline{\boldsymbol{u}} = [\overline{u},\overline{v}]^T,$$

then, we can say that, $\Delta x = \overline{u}t$ and $\Delta y = \overline{v}t$, giving us approximately,

$$\begin{aligned} \hat{\phi}_i^n &= \omega_i t - \phi_i^0 - \frac{\partial \phi_i}{\partial x}\overline{u}t - \frac{\partial \phi_i}{\partial y}\overline{v}t, \\ &= \left(\omega_i - \frac{\partial \phi_i}{\partial x}\overline{u} - \frac{\partial \phi_i}{\partial y}\overline{v}\right)t - \phi_i^0. \end{aligned} \tag{5}$$

Equation 5 shows that the angular frequency in the meridional velocity series of the buoy is shifted by a factor dependent on the phase gradients and the average buoy velocities.

Since the buoy is moving in a tidal wave, the buoy net phase $\left(\hat{\phi}_i^n\right)$ can be compared to the phase in a traveling wave with a wavenumber.

Considering the phase gradients are the wavenumbers projected on the x and y directions, that is, $k_{i_x} = \frac{\partial \phi_i}{\partial x}$ and $k_{i\,y} = \frac{\partial \phi_i}{\partial y}$. Then, Equation 5 can be re-written as:

$$\begin{aligned} \hat{\phi}_i^n &= \left(\omega_i - k_{i_x}\overline{u} - k_{i\,y}\overline{v}\right)t - \phi_i^0, \\ &= \left(\omega_i - \boldsymbol{k}_i.\overline{\boldsymbol{u}}\right)t - \phi_i^0 = \left(\omega_i - \Delta\omega_i\right)t - \phi_i^0. \end{aligned} \tag{6}$$

where $\boldsymbol{k_i}$ is the directional wavenumber of the wave corresponding to the i^{th} TCC. Although a wavenumber is a scalar quantity, for a tidal wave propagating in a particular direction on the globe, it can be decomposed into longitude (x) and latitude (y) directions with their respective wavenumbers.

From Equation 6, it becomes apparent that the tidal harmonics in the buoy velocity time series are shifted by a factor of $\Delta\omega_i(=\boldsymbol{k}_i.\overline{\boldsymbol{u}})$. It should be noted that traditional tidal analysis uses a model Equation 2 that is based on fixed and known tidal frequencies. If the above shift is significant, performing a traditional tidal harmonic analysis on the buoy data directly using the list of tidal harmonics ({TH}) will lead to erroneous results. This issue arises because the harmonic analysis attempts to fit to standard tidal frequencies in the buoy velocity times series, whereas, these frequencies are actually shifted.

The shift is significant when the order of magnitude of $\boldsymbol{k}_i.\boldsymbol{u}$ is comparable or larger than ω_i, which can be evaluated by a simple scaling analysis. For M_2 and S_2 constituents $\omega_i \sim 10^{-4}\text{rad/s}$. Considering an average buoy velocity of 1m/s, the wavenumber (k_i) can be estimated using the underlying tidal wavelength (λ_i) via their inverse relationship. For barotropic tidal waves, the wavelengths are in the order of 1000 km, making the shift negligible. On the other hand, for baroclinic tidal waves, the order of wavelengths ranges from 10 km to 1000 km (Apel, 2003; Simmons et al., 2004), and the shift can be in the order of the tidal frequency making it significant. These shifts are similar to the Doppler shift phenomenon where the buoy is moving in a medium (i.e., the tidal wave).

2.3. Model-Derived Fitting Method

For TCC estimations from single buoy trajectories, it is imperative to address challenges arising from the space-time variation of amplitudes and phases. This variability can be approximated by a first-order Taylor Series expansion:

$$H_i(x,y,t) \approx H_i(x_0,y_0) + \left.\frac{\partial H_i}{\partial x}\right|_{(x_0,y_0)}(x-x_0) + \left.\frac{\partial H_i}{\partial y}\right|_{(x_0,y_0)}(y-y_0), \tag{7}$$

$$\phi_i(x,y,t) \approx \phi_i(x_0,y_0) + \left.\frac{\partial \phi_i}{\partial x}\right|_{(x_0,y_0)}(x-x_0) + \left.\frac{\partial \phi_i}{\partial y}\right|_{(x_0,y_0)}(y-y_0), \tag{8}$$

Where the subscript 0 denotes the values at the start of the buoy trajectory. By substituting in Equation 2, we obtain:

$$u_t(x,y,t) = \sum_{i\in\{\text{TH}\}} H_i^{\,0}\cos\left(\omega_i t - \phi_i^{\,0} + \nabla_{\boldsymbol{\phi}_i}\cdot\boldsymbol{\Delta}\mathbf{x}\right) + \nabla_{\boldsymbol{H}_i}.\boldsymbol{\Delta}\mathbf{x}\cos\left(\omega_i t - \phi_i^{\,0} + \nabla_{\boldsymbol{\phi}_i}\cdot\boldsymbol{\Delta}\mathbf{x}\right), \tag{9}$$

where the gradients, $\nabla_{\boldsymbol{\phi}_i}$ and $\nabla_{\boldsymbol{H}_i}$, are the gradient vectors evaluated at (x_0,y_0), and the dot product is taken with the displacement vector $\boldsymbol{\Delta}\mathbf{x} = \left[(x-x_0),(y-y_0)\right]^T$.

Likewise, a similar equation for the v_t component is given by:

$$v_t(x,y,t) = \sum_{i\in\{\text{TH}\}} G_i^{\,0}\cos\left(\omega_i t - \theta_i^{\,0} + \nabla_{\boldsymbol{\theta}_i}\cdot\boldsymbol{\Delta}\mathbf{x}\right) + \nabla_{\boldsymbol{G}_i}.\boldsymbol{\Delta}\mathbf{x}\cos\left(\omega_i t - \theta_i^{\,0} + \nabla_{\boldsymbol{\theta}_i}\cdot\boldsymbol{\Delta}\mathbf{x}\right), \tag{10}$$

where the gradients, $\nabla_{\boldsymbol{\theta}_i}$ and $\nabla_{\boldsymbol{G}_i}$, are the gradient vectors evaluated at (x_0,y_0).

Equation 9 has the same form as the equation used for tidal estimation in Lie et al. (2002), which employs a linear polynomial for amplitude and phase. This implies that the coefficients of the polynomial in the method from Lie et al. (2002) represent derivatives of amplitudes and phases, with first-order derivatives for a linear polynomial, second-order for a quadratic polynomial, and so on.

However, for a single buoy in the case of a unidirectional flow, attempting to estimate the gradient in the orthogonal direction would result in a singular matrix implying an ill-conditioned problem, leading to erroneous estimations of amplitude and phase. This issue could also affect the method by Kodaira et al. (2016), which utilizes a third-order polynomial. Nonetheless, these methods may perform adequately due to the averaging of estimates from numerous buoys within a region or grid cell.

Additionally, adopting a linear polynomial approximation necessitates estimating six parameters per TCC: the initial amplitude and phase, along with their gradients in both the x and y directions. If {TH} includes n constituents, then $6n$ parameters must be estimated, significantly more than the $2n$ parameters in standard tidal harmonic analysis. This increased parameter count necessitates a trajectory with a high sampling frequency, that is, a large number of data points. The complexity of estimation escalates with the polynomial order.

In the newly proposed, Model-derived Fitting Method (reffered to as MdF henceforth), as the name implies we capitalize on a tidal model to obtain initial estimates of the amplitudes and phases (Equations 7 and 8). Consequently, we have:

$$H_i(x,y,t) = \alpha_i H_i^m(x,y,t), \tag{11}$$

$$\phi_i(x,y,t) = \phi_i^m(x,y,t) + \beta_i, \tag{12}$$

Where H_i^m and ϕ_i^m are the amplitude and phase of TCC i obtained from a tidal model at location x, y. Tidal models, particularly in the Arctic, have limited accuracy. The parameter α_i is the multiplicative correction applied to the amplitude derived from the model, and parameter β_i is the additive correction to the phase for each TCC. Here, we assume these parameters are constant over the region covered by the buoy trajectory. This results in $2n$ parameters to estimate which is same as a standard tidal harmonic analysis.

Substituting this into Equation 2, we obtain:

$$u_t(x,y,t) = \sum_{i\in\{\mathrm{TH}\}} \alpha_i H_i^m(x,y,t)\cos\left(\omega_i t - \phi_i^m(x,y,t) + \beta_i\right), \tag{13}$$

These parameters can be estimated through a least squares fit with the resulting cost function given by:

$$J(\boldsymbol{q}) = \sum_{j=0}^{N} \left(u_t\left(x_j, y_j, t_j\right) - f\left(t_j, \boldsymbol{\omega}, \boldsymbol{\Delta}\mathbf{x}_j, \boldsymbol{q}\right)\right)^2, \tag{14}$$

where N equals the number of points in the velocity time series, f is a function representing the right-hand side of Equation 13, $\boldsymbol{\omega}$ denotes the vector of angular frequencies for the n TCCs, and $\boldsymbol{q}$ is the parameter vector with elements:

$$\boldsymbol{q} = \left[\alpha_i, \beta_i\right], i \in \{\mathrm{TH}\}.$$

To avoid unrealistic parameter values, we impose constraints on the parameters as follows:

$$0 \le \alpha_i \le C, \tag{15}$$

$$0 \le \beta_i \le 2\pi, \tag{16}$$

where the constant C is a maximum threshold value which we set as 5 in this paper. The maximum limit in the amplitudes has a notion that if the parameters reach this limit one can expect that the model amplitudes are significantly different than the truth and the method would benefit from a different model with better first approximation.

We can re-write Equation 13 as:

$$u_t(x,y) = \sum_{i\in\{\mathrm{TH}\}} \alpha_i \cos\left(\beta_i\right) H_i^m(x,y,t)\cos\left(\omega_i t - \phi_i^m(x,y,t)\right) - \alpha_i \sin\left(\beta_i\right) H_i^m(x,y,t)\sin\left(\omega_i t - \phi_i^m(x,y,t),\right. \tag{17}$$

$$= \sum_{i\in\{\mathrm{TH}\}} A_i H_i^m(x,y,t)\cos\left(\omega_i t - \phi_i^m(x,y,t)\right) - B_i H_i^m(x,y,t)\sin\left(\omega_i t - \phi_i^m(x,y,t)\right), \tag{18}$$

where A_i and B_i are the new parameters to be estimated for the i^{th} TCC. This is now a linear estimation problem in A_i and B_i and is akin to a tidal harmonic analysis, albeit with a different coefficient matrix. This matrix now includes an initial approximation of the amplitude and phase from the model.

By substituting the estimated parameters into Equation 13, one can determine the velocity in the region covered by the buoy trajectory as long as our approximation holds true. Additionally, given the parameters, we can compute the amplitude and phase of a TCC at a specific location in the region using Equations 11 and 12.

As with a regular tidal harmonic analysis, the number of parameters in this method is $2n$ but with constraints (Equations 15 and 16). This, along with obtaining initial approximations from a model and a reformalization as per Equation 18 lends this method robustness and suitability for operational purposes.

Note that the cost function Equation 14 is computed over the buoy trajectory at the true positions $((x, y, t))$ of the buoys. The initial estimates of the amplitudes and phases are obtained from the model at these positions $((x, y, t))$. Consequently, the space-time variations of the amplitudes and phases are implicitly incorporated into this method. These space-time-varying initial estimates, reflecting the changing buoy positions over time, inherently also account for the frequency shift (from Equation 6) due to mean currents.

The method focusses on estimation of a list of four principal TCCs. that is, $\{\mathrm{TH}\} = \{M_2, S_2, O_1, K_1\}$. Due to lack of knowledge of the signal-to-noise level of the buoy trajectories we use a simple Rayleigh criteria (Foreman & Henry, 1989) to select 15-day buoy trajectories for distinguishing these TCCs. A similar trajectory length in days has also been employed in Lie et al. (2002), Poulain and Centurioni (2015), Kodaira et al. (2016), which have noted that extended trajectories can lead to significant amplitude and phase variations.

3. Models and Data

3.1. Barotropic and Baroclinic Tidal Models

For the initial estimates in the MdF Method, we utilize tidal models suitable for the specific nature of tidal currents in the study areas. One barotropic and one baroclinic model are employed for regions with dominant barotropic and baroclinic tidal currents, respectively. The Arctic barotropic tide model employed is the Global Tide and Storm Surge Model (GTSMv4.1) (Verlaan et al., 2015). GTSMv4.1 is a global depth-averaged barotropic model forced by a full tide-generating potential, that is, all tidal constituents are included. It is developed within the Delft3D Flexible Mesh suite from Deltares, using an unstructured grid. The grid resolution varies, with 25 km in the open ocean and 2.5 km near coastal regions. The model utilizes the GEBCO2019 gridded bathymetry (GEBCO Bathymetric Compilation Group, 2019) which has been further calibrated globally in Wang et al. (2021).

The GTSM is governed by the depth-averaged shallow water equations and incorporates parameterizations of the Self-Attraction and Loading (SAL) and internal tidal wave drag (Irazoqui Apecechea et al., 2017). Additionally, the effects of Arctic sea ice dissipation on tides have been integrated into the model (Vasulkar et al., 2024). The GTSM data used in this research is drawn from runs for the year 2014 which contain only tides, and no wind forcing.

For the baroclinic region analysis, the Arctic Tidal Analysis and Forecast product was utilized (E.U. Copernicus Marine Service Information (CMEMS), 2018. This product operates on a 3D TOPAZ6 model, integrating atmospheric forcing from ECMWF IFS HRES and tidal boundary conditions from the FES2014 data set (Lyard et al., 2021). Outputs are provided on a 3 km × 3 km grid and include sea surface elevation and surface ocean currents, which are informed by ocean general circulation, wind-driven effects, and tidal currents, and available from 2018.

3.2. GNSS Buoy Data Sources

Arctic GNSS buoy data were sourced from a Barents Sea expedition and the IABP portal. In an expedition to the Barents Sea region in March 2014 (Kaleschke & Müller, 2022) an array of 15 drifting ice buoys were deployed. Termed as beacons by their manufacturer, they came equipped with a GNSS receiver that recorded buoy positions every 15 min. The details of the 15 buoys and their drifting trajectories are discussed in Vasulkar et al. (2022).

From the IABP, we utilized a LEVEL 1 data product (IABP, 2014) with a 3-hourly resolution, featuring different types of buoys operational from 1979 to 2016. The year 2014 had the highest number of operational buoys (327) in this data set. We selected a buoy from this data set that was operational in the western Chukchi Sea in 2014 (Figure 5). The data for this buoy had no gaps or quality issues during our study period and thus required no additional processing.

We also used a LEVEL 2 data product (IABP, 2018) for a buoy in Baffin Bay in 2018 (Figure 7). This product, encompassing data from 2015 to 2021, included a total of 329 buoys and underwent processing to remove “obvious spikes” and the beginning of the data record. The selected buoy from this data set exhibited no missing data.

3.2.1. Processing for Buoy Velocity Time Series

For all the buoys, a buoy-derived velocity time series was computed using a central difference approach. This series was then bandpass filtered with cutoff frequencies corresponding to periods of 10 and 30 hr to capture the tidal band currents (TBC) of the meridional (u_t) and zonal (v_t) components. For bandpass filtering we used a second order Butterworth filter and applied in both forward and backward directions to realise a zero-phase filter. This technique aligns with Poulain and Centurioni (2015) and Baumann et al. (2020). We employed the Hatyan tidal analysis and prediction software (Veenstra, 2023) to evaluate Equation 2 while computing the cost functions for the least squares.

3.3. Arctic Tidal Current Atlas

For robust validation, we leveraged the Arctic-wide tidal current atlas compiled by Baumann et al. (2020). This atlas aggregates data from 429 moored current measurements, primarily from Acoustic Doppler Current Profilers (ADCPs), collected over 2 decades (2000–2020). This comprehensive compilation provides predictions for tidal currents, TBC, and tidal ellipse parameters over a uniform depth grid. Additional details of the data used from this data set are provided later.

4. Study on Frequency Shift in Buoy Trajectories

4.1. Details of Experiment

The purpose of this analysis is to discern a possible frequency shift in buoy trajectories where we focus only on the dominant M_2 tidal frequency. To investigate this phenomenon, we examined the velocity time series (u_t and v_t) from two buoy trajectories. The first buoy trajectory is the Buoy Baf from the IABP data set located in the baroclinic dominant Baffin Bay (Figure 7). The second is Buoy 16 sourced from the Barents Sea data set (Figure 2).

Amplitude peaks of tidal currents near the M_2 frequency from these buoy trajectories are scrutinized in the frequency domain. To do this, we apply a Fast Fourier Transform (FFT). The magnitudes from the FFT are scaled by a factor of $2/N$, where N represents the number of points in the truncated velocity series, to obtain the amplitude spectrum. Peaks with values greater than 1 cm/s, within a range of ±2h from the M_2 frequency, are identified.

For buoys that exhibit peaks deviating from the M_2 frequency, these peak frequencies are compared to theoretical values derived from Equation 5, re-written as:

$$\hat{\phi}_i^n = (\omega_i + \Delta\omega_i)\,t - \phi_i^0, \tag{19}$$

where

$$\Delta\omega_i = -\frac{\partial\phi_i}{\partial x}\overline{u_t} - \frac{\partial\phi_i}{\partial y}\overline{v_t}. \tag{20}$$

The primary objective here is to ascertain if the magnitude of the observable shift in the M_2 frequency in the buoy spectrum corresponds to the magnitude of the theoretical frequency shifts, thus potentially validating our hypothesis. Here, we do not take into account the orientation (x or y) of the M_2 phase changes and direction of the current. Thus, the magnitude of average frequency shift can be given by:

$$\begin{aligned} |\Delta\omega_i| &= |k_i||\overline{u}|, \\ &= \frac{\omega_i}{c_i}|\overline{u}|, \end{aligned} \tag{21}$$

$$= \frac{2\pi}{\lambda_i}|\overline{u}|, \tag{22}$$

where $\overline{u}$ is the average buoy velocity, c_i is the tidal wave speed and λ_i is the wavelength for the TCC $i \in \{\text{TH}\}$.

The net angular frequency $\left(\omega_i^n\right)$ tracked by the buoy is then,

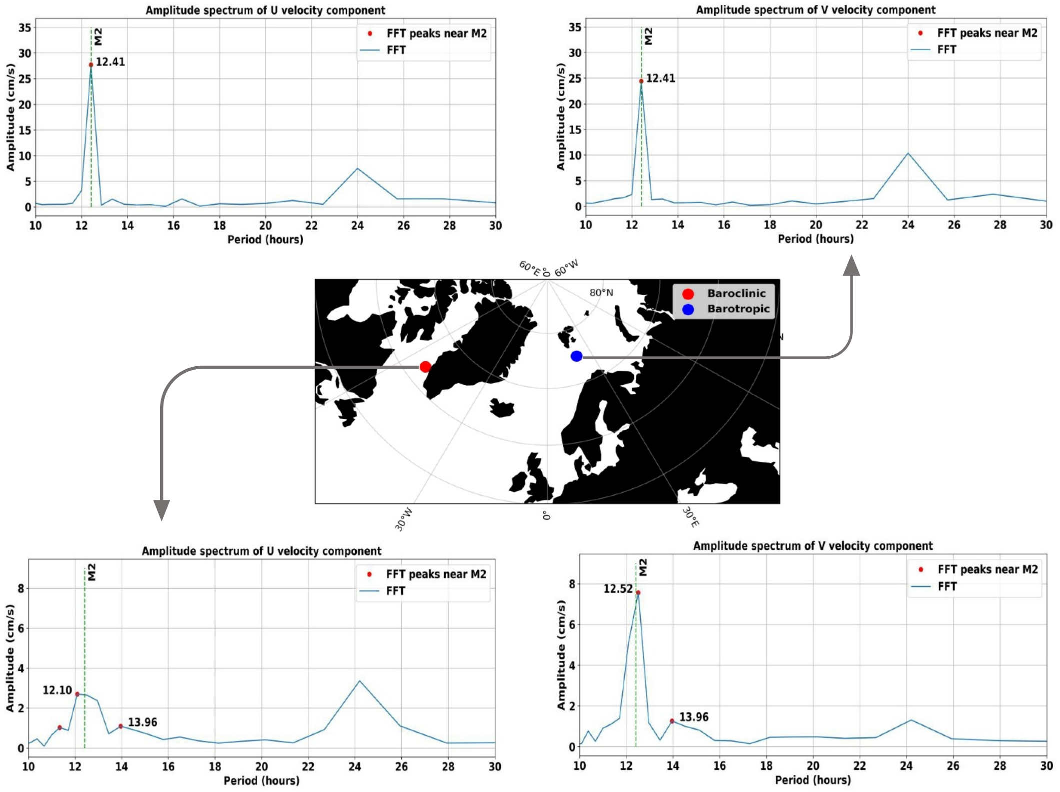

Figure 1. Depiction of the median location of the two buoy trajectories analyzed in this study. The blue dot represents the buoy in the predominantly barotropic tidal current region, while the red dot represents the buoy in the baroclinic dominant region. The arrows point to the Fourier spectra of their amplitudes: the top two are for the barotropic buoy and the bottom two for the baroclinic buoy. The amplitude spectra for the u_t and v_t components of the buoy velocities are shown with a dotted green line marking the M_2 frequency. Peaks and their respective frequencies near the M_2 frequency are highlighted with red dots and annotations.

$$\omega_i^n = \omega_i \pm \frac{2\pi}{\lambda_i}|\overline{u}|. \tag{23}$$

Here, a positive (+) or negative (−) shift depends on the direction of the gradients. Using this equation, we can compute the new shifted frequencies and their corresponding time periods in both positive (added to the time period) and negative (subtracted from the time period) directions.

We are analyzing the M_2 tidal wave, which has a period of 12.42 hr. Since the wavelengths or the wave speed of the M_2 tidal wave in the region of the buoys are unknown, we analyze the average theoretical frequency shifts using Equation 22 for a range of wavelengths from 50 to 1,000 km. This range facilitates the analysis of behavior in the presence of baroclinic tides until it reaches the limit of barotropic tides around the wavelength of 1,000 km. Additionally, examining this range aids in determining the magnitude range of the frequency shift.

4.2. Results and Discussion

Figure 1 illustrates the positions of two buoys, alongside the spectra of their u_t and v_t velocity.

A clear observation from the spectrum of the buoy in the region with barotropic tidal currents (top two of Figure 1) reveals that both u_t and v_t velocities peak precisely at the M_2 frequency, suggesting no shift. Conversely, in the baroclinic dominant tidal region, the peaks for both u_t and v_t trajectories are displaced from the M_2 frequency. Specifically, the u_t component peaks at a time period of 12.10 hr (a negative shift from M_2), while the v_t component peaks at 12.51 hr (a positive shift from M_2). The other peaks shown in the u_t and v_t spectrum of the buoy in baroclinically dominant region are possibly the shifts from nearby TCCs apart from M_2.

Table 1
Theoretical Shifts in Hours (Computed Using Equation 23) of the M_2 Tidal Period for u_t and v_t Components for the Buoy in Baffin Bay

	Positive period shift		Negative period shift	
λ (km)	Value	Shift	Value	Shift
50	14.45	2.03	10.90	−1.52
100	13.36	0.94	11.60	−0.82
300	12.72	0.3	**12.13**	−0.29
1,000	**12.51**	0.09	12.33	−0.09

Note. The values in bold correspond to the shifts which are observed in Figure 1.

From Table 1 we can note that the average theoretical shifts corresponding to range of wavelengths less than 1,000 km align well with the observed shifts in the spectrum for the buoy in Baffin Bay. This shows that the theoretical shifts have similar order of magnitudes as the observed shifts.

In the barotropic case, which is modeled by linearized shallow water equations, one can approximate the wave speed as $c_i = \sqrt{gD}$, where g is the acceleration due to gravity and D is the water depth (Gill, 1982). At the median location of the buoy, the water depth as obtained from GEBCO2019 is approximately 50 m. Using this value, $c_i = 22.36$ m/s for this buoy, and the shift using Equation 21 can be evaluated. The resulting shift was negligible (<0.001h) which aligns with the observed result of no shift for the buoy.

In both regions, M_2 is the dominant tidal forcing (Kodaira et al., 2016; Pease et al., 1983; Vasulkar et al., 2022). However, the spectrum of the buoy in Baffin Bay (red dot) exhibits peaks at frequencies other than M_2. This indicates that although the external forcing is primarily M_2, additional peaks at nearby, non-tidal frequencies emerge. We attribute this observed M_2 frequency shift to the Doppler Shift effect (as discussed in Section 2.2.2), which can be approximately calculated using Equation 22. The magnitude of this frequency shift is inversely proportional to the M_2 tidal wavelength in the region. As a result, in areas where barotropic tides with large wavelengths dominate, such as the Barents Sea, the frequency shift becomes negligible. However, in regions with strong baroclinicity with smaller wavelengths, significant frequency shifts are likely to occur. Furthermore, these shifts suggest that applying traditional tidal harmonic analysis, which performs curve fitting by assuming a known M_2 frequency, might lead to erroneous estimations, as the actual spectrum displays peaks at frequencies different from the assumed M_2 tidal frequency.

5. Case Studies in Three Regions

5.1. Case 1: Barents Sea-Barotropic

5.1.1. Details of the Experiment

From the Barents Sea expedition data set (Section 3.2), we selected two trajectories of CALIB (Compact Air-Launched Ice Beacons) sea ice buoys for analysis (Figure 2). These buoys, located on ice, were drifting in a free drift ice field between Hopen and Bear Island in the Barents Sea, an area characterized by barotropic tidal currents (Baumann et al., 2020). Both buoys were operational during the same 15-day period from 1 to 15 May 2014.

To assess the accuracy and robustness of our TCC estimation method, we initially compared the tidal velocities estimated by our method against the actual velocities derived from the buoy data. This comparison also involved GTSM outputs, with the Root Mean Square Error (RMSE) serving as a quantitative metric for the analysis.

Given both buoys operated within the same region, we compared the analysis at a *comparison point* (as shown in Figure 2) instead of the median location for each buoy separately to reduce the impact of the spatial variability. Here, we evaluated the estimates from the MdF method applied to both buoys against GTSM outputs. This analysis included the computation of tidal ellipses for the four principal TCCs–M_2, S_2, O_1, and K_1. The computation of these current ellipses is facilitated by the amplitudes and phases of the u_t and v_t components, following the procedure outlined by Zhigang (2002). Note that we have also applied the MdF method for this case study using FES2014b data to ascertain the robustness of the method and the results are available in Appendix A. Furthermore, the exact values of the TCC estimates with both FES2014b and GTSM results are provided in Appendix B.

5.1.2. Results and Discussion

Figures 3a and 3b illustrate the meridional (u_t) and zonal (v_t) components of the tidal currents for Buoys 03 and 16, respectively. The RMSE values between buoy-observed tidal velocities and GTSM-derived tidal currents are [0.1 m/s, 0.11 m/s] for Buoy 03 and [0.15 m/s, 0.16 m/s] for Buoy 16 where the values in the vectors correspond to u_t and v_t components, respectively. The fit of the MdF estimated tidal currents has almost 50% lower RMSE of

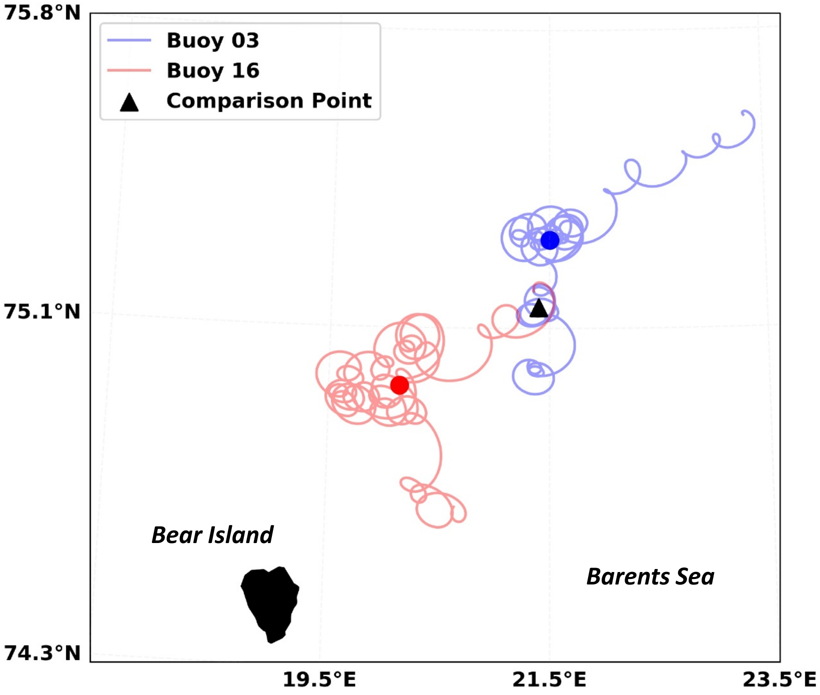

Figure 2. Trajectories of two buoys in the Barents Sea region near Spitsbergen Shelf (between Hopen and Bear Island) during 1–15 May 2014, recording data at a 15 min interval. The red and blue dots represent the median location of each buoy's trajectory. The black triangle indicates the comparison point at (21.4°E, 75.15°N), covered by both trajectories.

$[0.05\ \mathrm{m/s}, 0.07\ \mathrm{m/s}]$ for Buoy 03 and $[0.07\ \mathrm{m/s}, 0.08\ \mathrm{m/s}]$ for Buoy 16. The lower RMSE is expected as the GTSM currents are used as initial values for the estimation which is then optimized making use of the buoy data.

Furthermore, it is seen that the GTSM currents have smaller amplitudes than the buoy-observed estimates in all 4 panels that is, u_t and v_t for Buoy 03 and 16. On the other hand, the estimates from MdF have larger amplitudes than the buoy-observed currents. The signal of the buoy-observed data seems to be predominantly tidal.

The tidal current ellipses presented in Figure 4 offer a comparative view of the tidal current estimations from our MdF method applied to Buoys 03 and 16 and the corresponding values from the underlying GTSM.

For the M_2 constituent, semi-major axis estimates from MdF method for both the buoys are approximately 0.1 m/s larger than GTSM values, with Buoy 16 exhibiting the highest estimates. In the case of the S_2 and K_1 constituents, the values from Buoy 03 align more closely with GTSM, while Buoy 16's values are marginally higher $\approx$0.01 m/s. Notably, both MdF estimates consistently indicate the same directional trends as observed in the GTSM data, lending confidence to our method. However, for the O_1 constituent, there is little coherence between the estimates and the GTSM, with semi-major axis values falling below 0.01 m/s, which suggests lower confidence in these particular estimates.

It is important to note that the comparison point lies near the critical latitude for the M_2 constituent. At these latitudes, the frequency of M_2 is very close to the inertial frequency, making the decoupling of tidal and inertial signals particularly challenging (Pease et al., 1983; Vasulkar et al., 2022). In this context, the approximately 0.1 m/s higher amplitude observed in the buoy-derived estimates relative to GTSM for the M_2 constituent could be partly attributed to inertial oscillations. As discussed by Hasselmann (1970), inertial oscillations—typically characterized by amplitudes on the order of 0.1 m/s—can alias into the tidal frequency band when their frequency approaches that of the tidal signal. Since the GTSM does not account for wind effects and thus lacks the representation of inertial motions, the model inherently produces lower amplitude estimates for M_2. Moreover, it is also possible that the surface currents observed by the buoys could be slightly higher than the depth-averaged currents in GTSM, further contributing to this discrepancy.

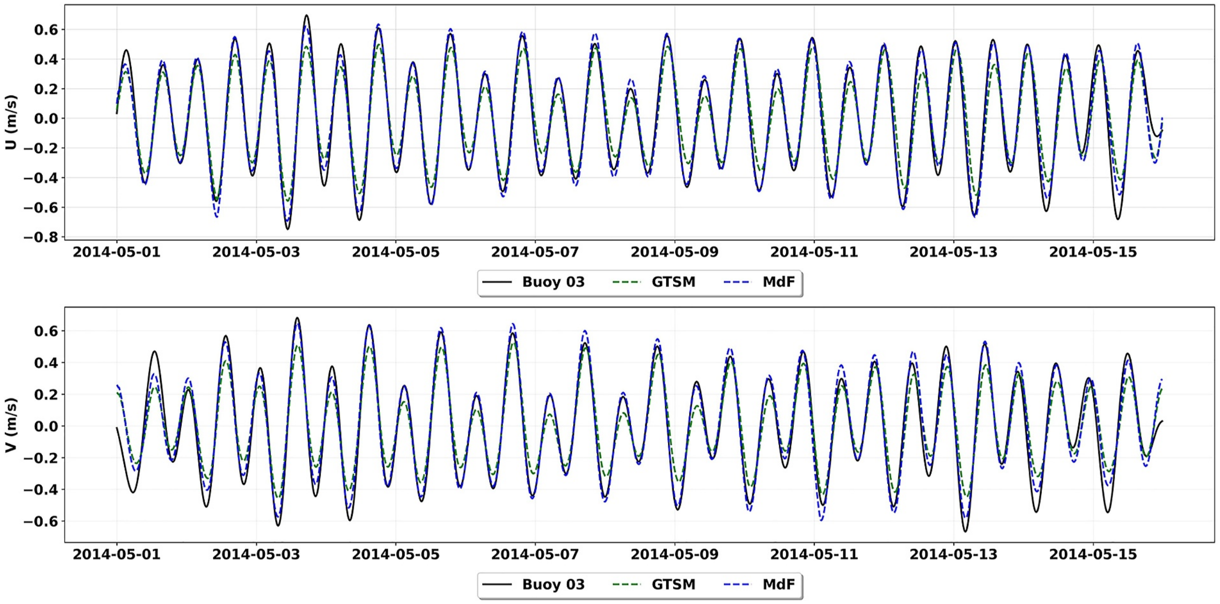

(a) BUOY 03

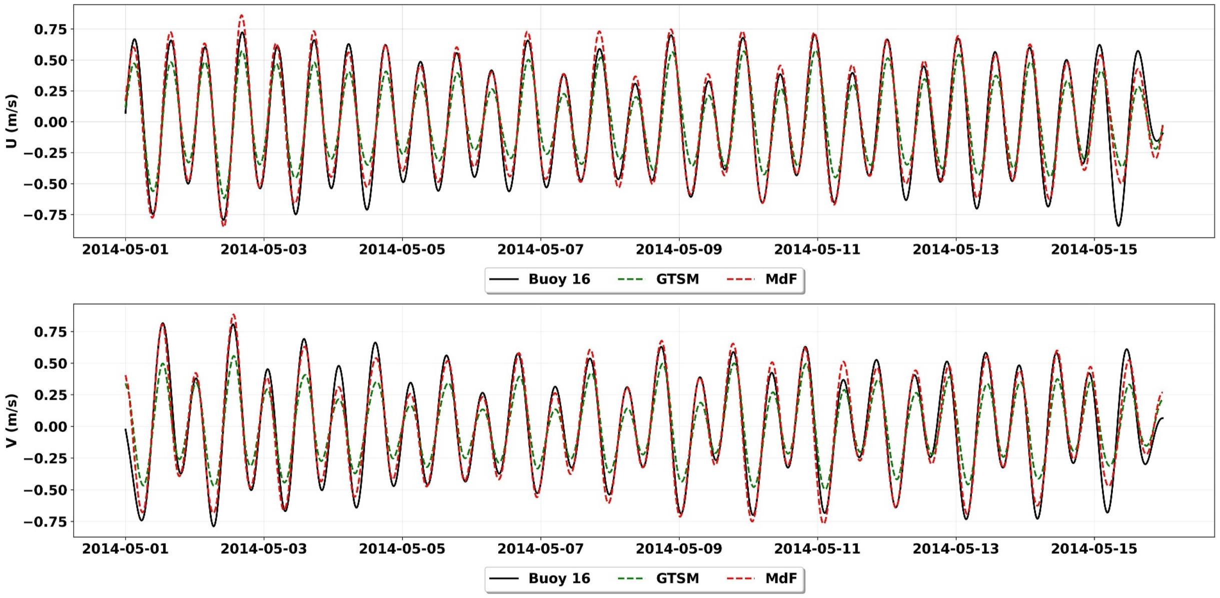

(a) BUOY 16

Figure 3. Comparison of tidal current velocities for Buoys 03 (a) and 16 (b) over a 15-day period starting 1 May 2014. The plots display the meridional (u_t) and zonal (v_t) bandpass-filtered velocity components derived from buoy observations alongside the values from GTSM (green) and the estimates from the MdF method. Note that the red and blue colors correspond to the respective Buoy 03 and Buoy 16 from Figure 2 while the black is for the observed tidal currents from the buoys.

Regarding the O_1 constituent, random and systematic error in the receiver positions may contribute to the incoherent results. Given the 15 min sampling interval and an average speed of 0.01 m/s, the resultant travel distance is approximately 9 m. This distance may fall below the GNSS receiver's threshold of accuracy, leading to uncertainties in estimations, especially for low-value measurements. However, without specific details on the

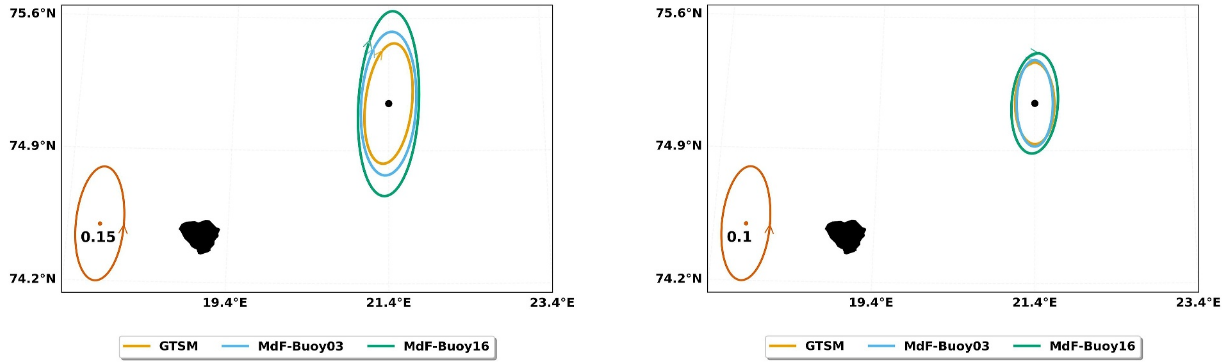

(a) M2 **(b) S2**

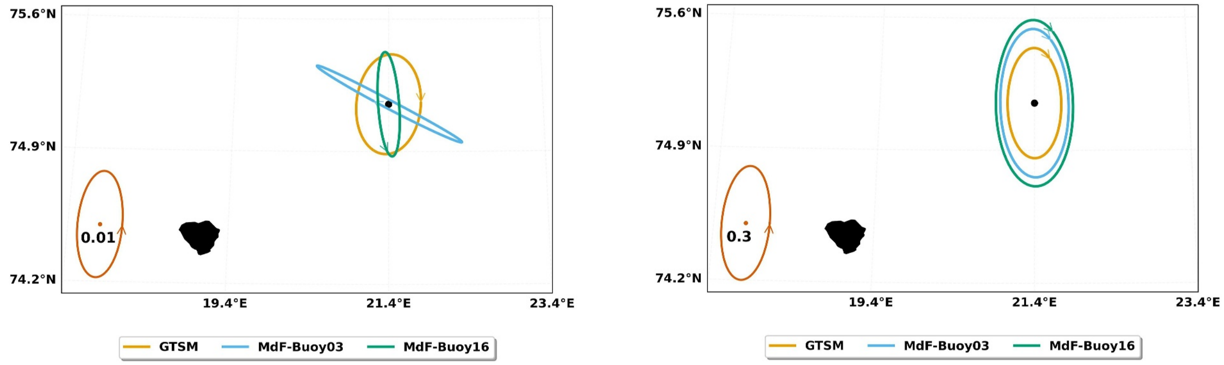

(c) O1 **(d) K1**

Figure 4. Tidal current ellipses for the 4TCCs-M_2 (a), S_2 (b), O_1 (c), K_1 (d). The center of the ellipse indicates the comparison point (21.4°E, 75.15°N); arrows on the ellipse represent its rotation. The comparison is between GTSM (orange), MdF applied to Buoy 03 (sky blue) and MdF applied to Buoy 16 (bluish green). The lower-left ellipse demonstrates the scale, with the magnitude of the semi-major axis given at the center in m/s.

GNSS receiver's instrument accuracy, we can only hypothesize about the nature of these errors. Systematic errors may also arise during phase estimation, particularly since O_1's amplitudes are an order of magnitude lower than those of other constituents. To ensure the analysis remains coherent and minimize uncertainties, here, we establish a criterion that any TCC with a semi-major axis less than 0.01 m/s will not be considered for comparison. This decision helps avoid potential inaccuracies associated with such low-value estimations, thereby enhancing the robustness of the analysis.

The quality of the fit of the MdF estimates along with its good agreement with GTSM values for the both the buoys at the comparison point sheds light on its accuracy and robustness. The marginally larger values observed in Buoy 16's estimates could be attributed to its more distant median location from the comparison point, as seen in Figure 2.

5.2. Case 2: Chukchi Sea-Barotropic

5.2.1. Details of the Experiment

In this study, the data from Chukchi Sea buoy, referred to as *Buoy Chuk* (Figure 5), was obtained from the IABP's LEVEL 1 data product for 2014. It had a sampling interval of 3 hours during the period 1 July to 15 July. Mounted on an ice floe, this surface velocity profiler buoy, with ID *300234061367150*, traversed the region west of Hanna Shoal, known for its predominantly barotropic tidal currents (Fang et al., 2022).

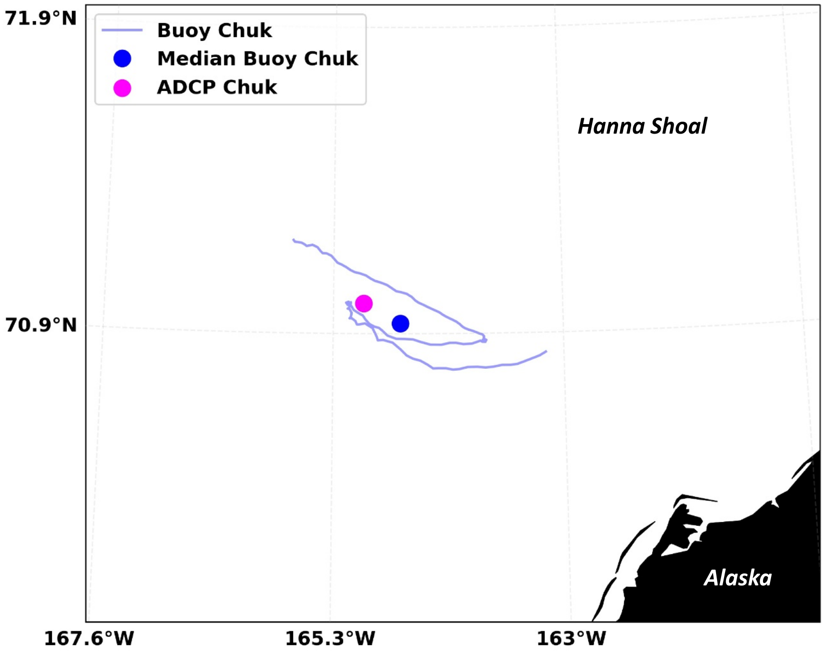

Figure 5. Trajectory of *Buoy Chuk* in the barotropically dominant region west of the Hanna Shoal in the Chukchi Sea. The median location of the Buoy Chuk (blue dot) and the nearby moored observation point from the Arctic Tidal Atlas (see Section 3.3) are also shown.

The Buoy Chuk was chosen for its complete data set, noting its drift through a free drift ice field with ice concentrations ranging from 0 to 0.8, as confirmed by sea ice data from Copernicus Marine Service (2014). Another selection criterion was the Buoy Chuk's proximity to a nearby ADCP mooring (*ADCP Chuk*), situated at a geodesic distance of 15.2 km from the Buoy Chuk's median location and intersecting its trajectory, thereby providing a valuable independent observation for validation purposes.

We evaluate the accuracy of the tidal estimates from our MdF approach on Buoy Chuk using GTSM as the underlying model. The TCCs from GTSM were derived from the simulations corresponding the Buoy Chuk's operational period (1–15 July 2014). In this case, since the comparison is at the Buoy Chuk's median location, we also use TTide (Pawlowicz et al., 2002) to compute the TCCs using the Buoy Chuk's velocity time series. For validation, we obtained the tidal ellipse parameters from the Full Record (FR) data of the ADCP Chuk and averaged it over the depth. This depth-averaged FR data from the tidal current atlas is suitable for comparison with barotropic TCCs as suggested by Baumann et al. (2020).

The analysis focuses on the M_2 tide, predominant in this region, and excludes other constituents since their amplitudes are below 8 mm/s. Tidal ellipses for the M_2 constituent are plotted at both the ADCP location and the Buoy Chuk's median location for visual comparison. For a quantitative assessment, the Vector Difference (VD) is calculated by comparing the buoy-derived and GTSM estimates at the mooring location against the mooring values. The VD is defined by Provost et al. (1995):

$$\mathrm{VD}_i = \sqrt{\left(A_i^o \cos\left(\phi_i^o\right) - A_i^e \cos\left(\phi_i^e\right)\right)^2 + \left(A_i^o \sin\left(\phi_i^o\right) - A_i^e \sin\left(\phi_i^e\right)\right)^2}, \tag{24}$$

where VD_i stands for the vector difference between the observation (represented by superscript o) and the estimated values from our methods (denoted by superscript e) for each TCC $i \in \{\mathrm{TH}\}$.

Note that the results of this study are also conducted with FES2014b model output and are available in Appendix A.

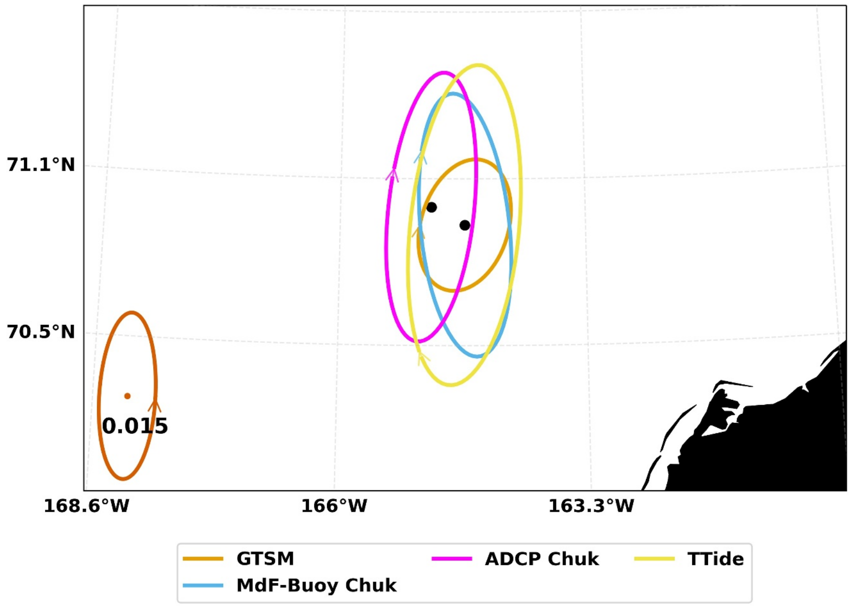

Figure 6. Tidal current ellipses for the M_2 constituent in the Chukchi Sea region. The ellipse's center indicates the data set's location, arrows on the ellipse represent its rotation, while the ellipse's color denotes the data set type. The lower-left ellipse demonstrates the scale, with its semi-major axis measuring 0.015 m/s.

5.2.2. Results and Discussion

Figure 6 presents tidal current ellipses for the M_2 tide at the median Buoy Chuk location and the mooring site (ADCP Chuk). Amplitudes, phases, and vector differences (VD) at the mooring location can be found in Table 2.

The GTSM values for the meridional component closely match the moored observations in amplitude and phase. However, the GTSM values for the zonal component are noticeably less than those from ADCP Chuk, leading to a reduced semi-major axis in GTSM's tidal ellipse. In contrast, the MdF's estimates for Buoy Chuk show a better resemblance to ADCP Chuk for both zonal and meridional components, as indicated by the smaller VD compared to GTSM. The tidal ellipse from the MdF method is similar to those from ADCP Chuk but displays a slight angular offset, likely due to the approximate 5° phase disparity in the zonal component. The VDs with MdF are less than 0.01 m/swhich are quite small given that these are based on a single buoy.

The corresponding tidal ellipse for M_2 using TTide yields amplitudes and phases that deviate significantly from the moored ADCP observations—particularly in the meridional component, where the phase offset is quite large. This is reflected in the larger vector differences (VD) of up to 0.036 m/s, as opposed to the much smaller VDs (≈0.003 m/s) obtained with the MdF method. These discrepancies likely stem from the short, 15-day Buoy Chuk record and the non-stationary Buoy Chuk path, both of which challenge standard harmonic analysis assumptions. Here, we hypothesize that energy from other tidal frequencies may appear at the M_2 tidal frequency due to aliasing.

Table 2
Comparison of the M_2 TCC Estimates at the ADCP Chuk Location

	u_t			v_t		
	H (m/s)	ϕ (deg)	VD (m/s)	H (m/s)	ϕ (deg)	VD (m/s)
ADCP Chuk	0.022	161.0	–	0.026	59.7	–
GTSM	0.025	165.0	0.004	0.012	88.8	0.017
Buoy Chuk	**0.025**	**160.0**	**0.003**	**0.023**	**54.9**	**0.003**
TTide	0.031	217.1	0.026	0.028	141.4	0.036

Note. MdF method is used for values in the row "Buoy Chuk" and VD is with respect to ADCP data. *H* is for amplitude, ϕ is for phase. The best values are bold for legibility.

In contrast, our MdF approach leverages model-derived spatio-temporal information and accounts for the Buoy Chuk's changing position, resulting in estimates that align more closely with the mooring data. Consequently, while TTide remains a robust tool for traditional, stationary records, its application to short and spatially varying buoy trajectories appears to be less reliable in this case study.

5.2.3. Discussion on Inertial Oscillations

The discrepancies observed—particularly the lower zonal amplitudes in GTSM—can, in part, be attributed to the influence of inertial oscillations. In the Arctic region, near the critical latitude for the M_2 constituent, the inertial frequency is very close to that of the tidal signal. As discussed by Hasselmann (1970), inertial oscillations with typical amplitudes around 0.1 m/s may alias into the tidal band, causing Buoy Chuk-derived estimates to exhibit slightly higher amplitudes compared to the model outputs. Since GTSM does not account for wind-induced inertial motions, its estimates are inherently lower. This effect is consistent with our earlier discussion in Section 5.1, where a similar inertial contribution was considered for the buoys in that study. Therefore, the absence of inertial oscillations in GTSM is a plausible explanation for part of its poorer performance relative to the MdF method, which appears to capture these effects more effectively.

Overall, while the potential aliasing of inertial oscillations remains an inherent limitation in the analysis of relatively short time series in this paper, the MdF method's ability to capture the direction of the ellipses and overall magnitude of the tidal signals supports its validity. Future work incorporating longer time series and additional observational data sets should help to further clarify and quantify the influence of inertial oscillations on tidal constituent estimates.

The examples in Sections 5.1 and 5.2 validate the TCC estimation of our MdF method, demonstrating its accuracy in Arctic regions with barotropic conditions. The method's robustness is evidenced by its model-derived estimates, which effectively capture spatio-temporal variability. This ensures consistent tidal estimates across different conditions. Furthermore, obtaining similar estimates from different buoys at the same location lends additional credibility to the method's robustness. The results are encouraging, but the number of collocation points we could find was very limited.

A broader validation, encompassing additional buoys across diverse Arctic regions, would ideally substantiate the reliability of our method for barotropic conditions. However, the harsh Arctic environment and the scarcity of independent validation data sets present significant hurdles to such expansive verification.

5.3. Case 3: Baffin Bay-Baroclinic

5.3.1. Details of the Experiment

Multiple factors influenced the selection of a buoy in the Baffin Bay region. Firstly, Baffin Bay is known for having tidal currents with strong baroclinicity (Baumann et al., 2020). Secondly, the 3D model TOPAZ6 data were available only from the year 2018. Thirdly, the arctic tidal atlas had one of the largest number of moorings in this region. Based on this, we selected a buoy in Baffin Bay, referred to as *Buoy Baf* (Figure 7).

It was sourced from the IABP's LEVEL2 data product (Section 3.2), featuring a 3-hr sampling interval from 28 October to 11 November 2018. The Buoy Baf's ID in the original data set is *300234064501660* which mentions that it was deployed with RV Atlante on 12 September 2018 at61.3°N and 28.2°W by the Atlantic Oceanographic and Meteorological Laboratory (AOML). This Buoy Baf is operating in open waters during a period typically free of sea ice in Baffin Bay based on sea ice concentration from GLORYS global reanalysis (Copernicus Marine Service, 2014).

Moorings named *ADCP Baf C4* and *ADCP Baf C6* (Figure 7) were selected based on their proximity to the buoy trajectory. TBC data, spanning the entire depth from these moorings, were obtained and computed through bandpass filtering with cutoff frequencies corresponding to periods of 10–30 hr (Baumann et al., 2020). At each location, the data set included TBC for five distinct durations.

5.3.2. Spatio-Temporal Variability of M_2 Tidal Ellipses in Baffin Bay

Technically, at the two locations of ADCP Baf C4 and ADCP Baf C6 in Figure 7, there were multiple expeditions to install ADCPs at approximately the same location over a number of years. Further technical details regarding these ADCP observations are found in Wu et al. (2013). From this data, we evaluate M_2 tidal ellipses by doing a tidal analysis on the TBC in the period from 28 October to 11 November and from 11 November to 28 November for the 5 years of data availability. The first 15-day period corresponded to the Buoy Baf period and the next 15-day period for 5 years was plotted to show the temporal variability. These M_2 ellipses are plotted for both the locations for the surface currents and the depth-averaged currents (Figures 8 and 9).

Significant temporal variability is observed at both locations for the surface tidal ellipses, with a standard deviation of approximately 5 cm/s. Conversely, the depth-averaged tidal ellipses exhibit a standard deviation of less than 1 cm/s. The mean values for depth-averaged currents are equal to or less than those for surface currents,

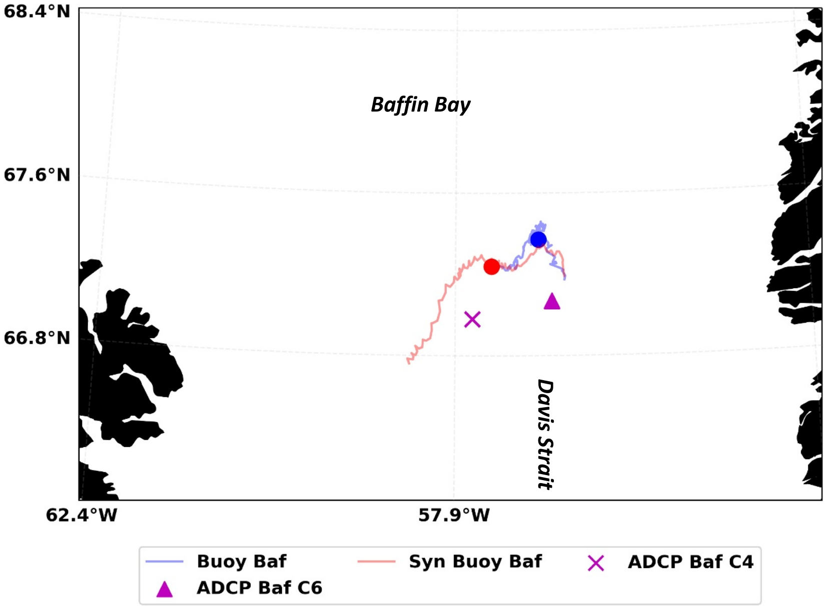

Figure 7. Trajectories and mooring observation locations in Baffin Bay. Trajectory period 28 October–11 November 2018 for Buoy Baf and the corresponding synthetic trajectory for the same period. The corresponding medians positions for the trajectories are given by dots. The ADCP mooring locations in magenta are for *ADCP Baf C4* and *ADCP Baf C6* data locations.

suggesting that surface tidal currents are stronger or equivalent to depth-averaged currents. Spatial variability in tidal currents is also evident, with ADCP Baf C4 displaying a larger semi-major axis compared to ADCP Baf C6.

To further illustrate the spatial aspect of this variability, Figure 10 shows the modeled M_2 amplitude contours for u_t and v_t components in Baffin Bay, using the barotropic model. The contours are spaced at 0.005 m/s intervals. Around the ADCP locations, relatively minimal color changes (i.e., small amplitude variations) align with the low standard deviations seen in Table 3. However, moving eastward, one can observe more pronounced amplitude gradients, underscoring the broader spatial heterogeneity in this region.

Overall, the substantial spatio-temporal variability in the surface tidal currents corroborates the presence of strong M_2 baroclinic tides. In such baroclinic zones, two main challenges emerge: significant temporal and spatial variability, and the potential mismatch between surface and depth-averaged currents. While a 3D tidal model might better capture vertical variations, coincident buoy and mooring observations remain crucial for accurately validating these dynamic conditions.

We applied the MdF method to the Buoy Baf trajectory and computed the M_2 tidal ellipse. This estimate was compared to the underlying 3D TOPAZ6 model and evaluated against the standard deviation observed at the nearby ADCP locations (Table 3). We also used TTide to compute the corresponding value for comparison. Note that there was no mooring observation in 2018 near the buoy location to validate.

5.3.3. Results-Real Buoy Data

Figure 11 illustrates the M_2 tidal ellipses, comparing the MdF estimates for Buoy Baf with those from TOPAZ6 and TTide estimates at the same location for 28 October to 11 November period. The Buoy Baf's estimated semi-major axis is 0.15 m/s, which falls within the standard deviation range reported in Table 3. In contrast, the TOPAZ6 estimate is about 0.2 m/s, exceeds that range. These findings suggest that the MdF estimate may be more realistic, although its true accuracy remains uncertain without direct observational validation.

Notably, when using TTide for harmonic analysis, the largest amplitudes in u_t and v_t appeared at the S_2 frequency rather than M_2. We attribute this shift to Doppler effects arising from the Buoy Baf's motion in baroclinically dominant region, which can redistribute part of the M_2 energy into neighboring frequencies.

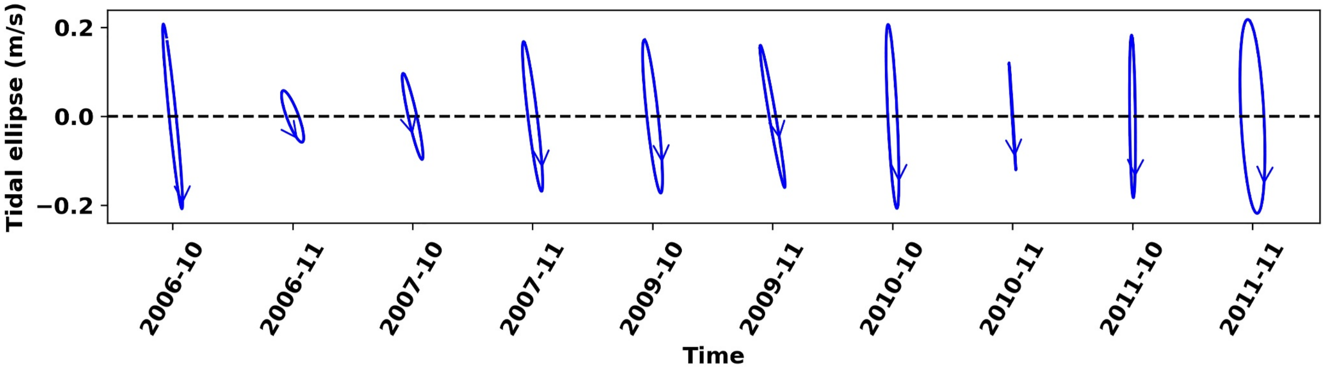

(a) Surface

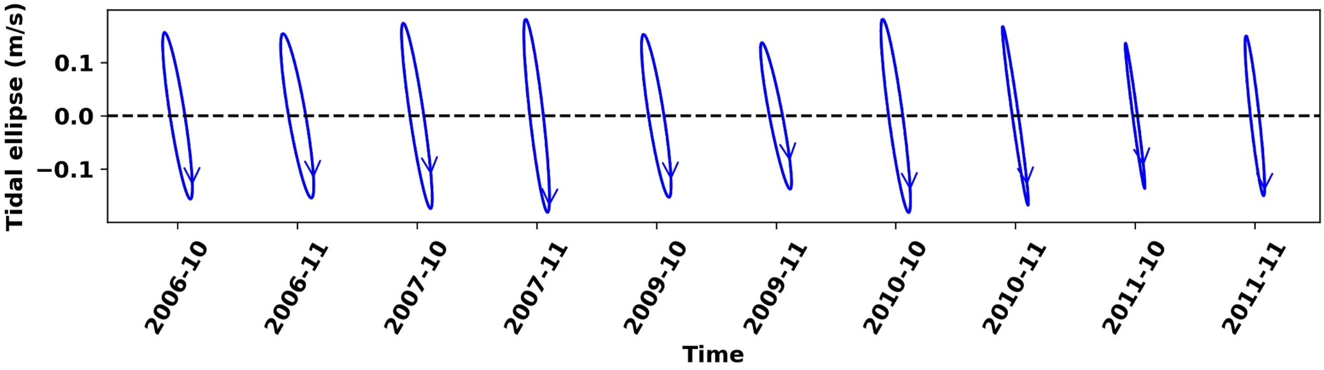

(b) Depth-averaged

Figure 8. Tidal ellipses of the M_2 constituent measured by mooring ADCP Baf C4. Panel (a) shows the surface component over time. Panel (b) shows the depth-averaged component over time.

The absence of a mooring data set at exact spatial location and temporal duration for validation in this baroclinically dominant Baffin Bay region with large spatio-temporal variability prompted us to conduct a synthetic test.

5.3.4. Synthetic Experiment

This experiment involved constructing a synthetic buoy (referred to as *Syn Buoy Baf*) trajectory using the following equation:

$$\frac{\partial \boldsymbol{x}}{\partial t} = \boldsymbol{u} + \boldsymbol{\epsilon}, \tag{25}$$

where $\boldsymbol{x}$ represents the Syn Buoy Baf's position vector, $\boldsymbol{u}$ is the surface velocity vector derived from the model (TOPAZ6), and $\boldsymbol{\epsilon}$ denotes a zero-mean Gaussian noise with standard deviation of 0.01 m/s.

This equation was integrated over time with a forward Euler scheme having a time step of 15 min. Integration, starting from the actual Buoy Baf's initial position ($\boldsymbol{x}_0$) on October 28, produces the Syn Buoy Baf trajectory (Figure 7) over a 15-day period. Since the underlying model is TOPAZ6, we obtain the TCC values at the median location of the Syn Buoy Baf from the model providing us with the *synthetic truth*.

Next, in the Baffin Bay region covered by the Syn Buoy Baf trajectory, we obtain TOPAZ6 model data for a subsequent 15-day period starting 12 November. Due to the temporal variability of baroclinic currents in this region, the new model data differs from that used to create the Syn Buoy Baf.

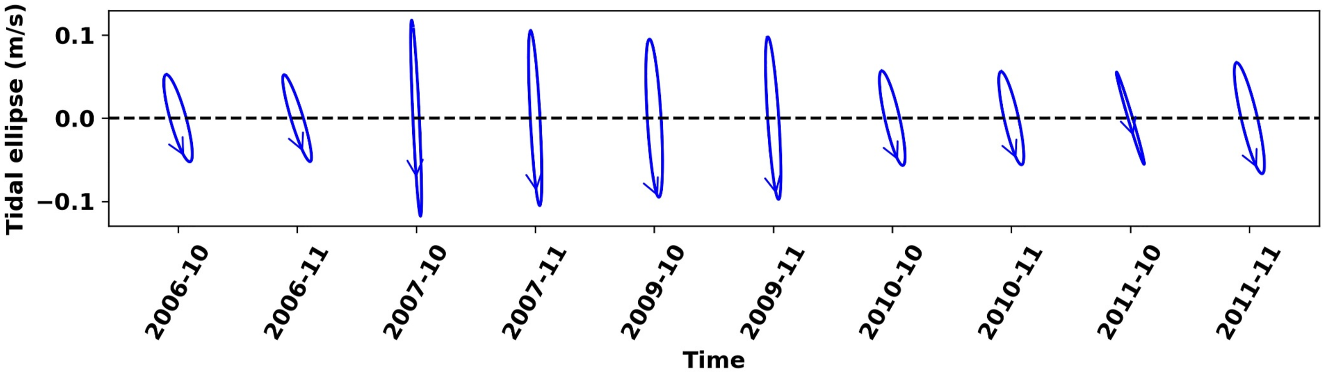

(a) Surface

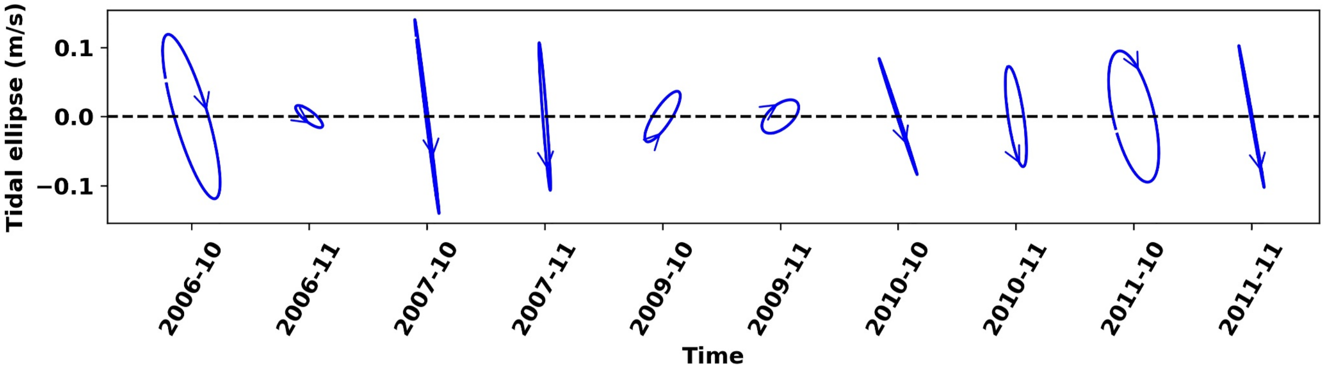

(b) Depth-averaged

Figure 9. Tidal ellipses of the M_2 constituent measured by mooring ADCP Baf C6. Panel (a) shows the surface component over time. Panel (b) shows the depth-averaged component over time.

Using this new TOPAZ6 data as the initial condition and the Syn Buoy Baf trajectory, we apply the MdF method to estimate the TCC parameters. These estimates are subsequently compared with the synthetic truth to evaluate the method's performance. Additionally, we apply TTide to perform a standard tidal harmonic analysis of the Syn Buoy Baf data for comparison. This assessment includes calculating tidal ellipses and vector differences, as described in Section 5.2.

5.3.5. Results and Discussion

Figure 12 shows the tidal ellipses for the synthetic truth, initial estimates from the TOPAZ6 model, TTide estimates for Syn Buoy Baf and MdF estimation from the Syn Buoy Baf. The vector differences (VD_i) relative to the synthetic truth are detailed in Table 4. The O_1 TCC is omitted since its amplitude is <1 cm/s.

The estimations from the MdF method using TOPAZ6 model data appear to be in close agreement with the synthetic truth values. There is a noticeable phase discrepancy of approximately 5–10° for the S_2 and K_1 constituents between the estimated and actual values, resulting in a slight angular difference between the ellipses. In contrast, the initial estimates from the TOPAZ6 model differ significantly from the synthetic truth, as evidenced by the larger vector differences.

The estimates from TTide differ significantly from the synthetic truth values with large VD. Notably the highest VD of 0.037 was observed for the v_t component of S_2 constituent. Upon observing the peaks in the tidal harmonic analysis, it was seen that the peak occurred at the S_2 frequency as opposed to M_2 frequency. We can interpret this discrepancy as indicative of a Doppler shift effect along the Syn Buoy Baf's trajectory. This reinforces the notion

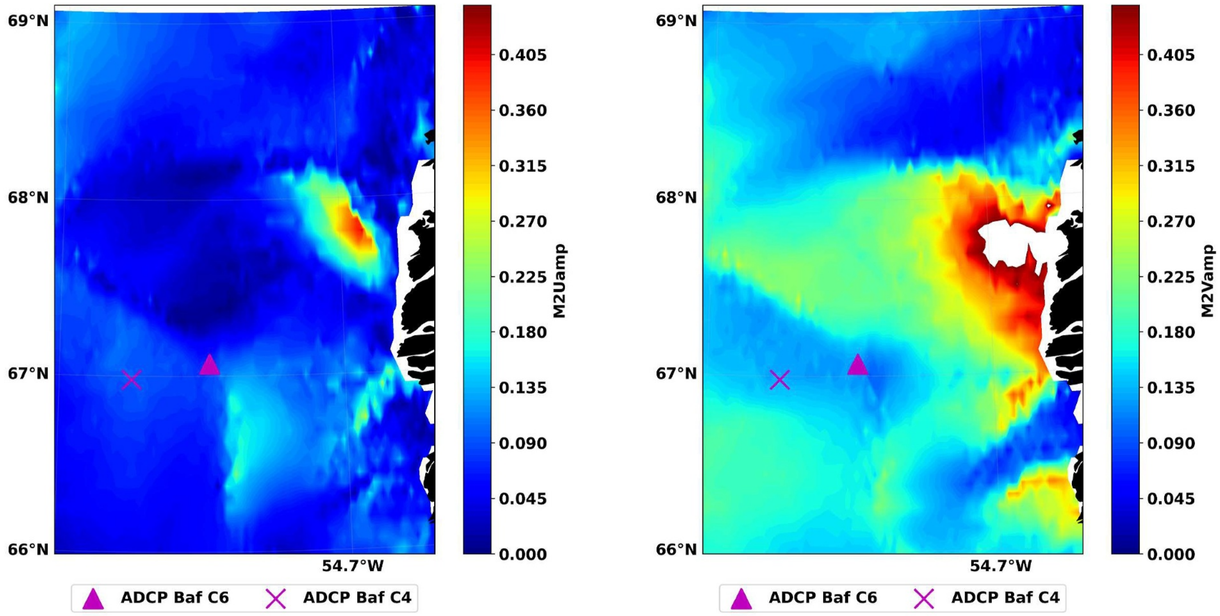

(a) M2 U Amplitude

(b) M2 V Amplitude

Figure 10. Amplitude contours of the M_2 tidal constituent from the barotropic model in Baffin Bay around ADCP locations. (a) U-component amplitude, (b) V-component amplitude. The ADCP locations Baf C6 and Baf C4 are marked with a triangle and cross, respectively. The contours have a resolution of 0.005 m/s.

that conventional tidal harmonic analysis may be inadequate for capturing the true TCC in such strong baroclinic cases with strong spatio-temporal variations in amplitudes and phases, thereby underscoring the advantage of our MdF method in such complex environments.

The MdF method's accuracy in the synthetic case suggests its applicability in regions with dominant baroclinic tides. Although this conclusion stems from a synthetic test, the outcomes imply that model-derived gradients in amplitude and phase can aid in accurately estimating tidal parameters from buoy trajectories. The substantial difference between the initial model estimates and the synthetic truth, coupled with the agreement between the synthetic buoy-derived estimates and the true values, lends credibility to the method's effectiveness.

Synthetic experiments enable the computation of realistic estimates of expected accuracy of the method by comparing against known truths within the simulation framework. However, the reliability of these estimates depends upon the accuracy of the uncertainties factored into the computation. Such experiments may yield overly optimistic results if the underlying uncertainties are not accurately represented.

A more definitive assessment of the MdF method's ability in baroclinic dominant regions would need a validation against independent observational data. Securing such a data set for baroclinic dominant regions, which must closely correspond in location and time with the model and buoy trajectory, remains a substantial challenge. Future opportunities to access such data would further validate the reliability and usefulness of these buoy-derived estimates in such complex regions.

Table 3
Variability of the Semi-Major Axis of M_2 Tidal Ellipses at the Two ADCP Locations Computed as Mean and Standard Deviation With Units in m/s

	Surface		Depth-averaged	
	Mean	Std.	Mean	Std.
ADCP Baf_C4	0.18	0.04	0.19	0.01
ADCP Baf_C6	0.16	0.05	0.12	0.009

The spatially constant correction factors (Equations 11 and 12), can only correct for errors already present in the underlying initial model estimates. If the underlying tidal models fails to resolve local features, the multiplicative and additive correction factors are merely a spatially averaged bias correction and cannot retrieve the small scale signal. Consequently, the estimates from this MdF method are ultimately bounded by the underlying tidal model.

Since this approach depends on reliable initial estimates from a model, it necessitates the availability of a model to derive estimates from buoy trajectories. This reliance forms a significant limitation in scenarios where such

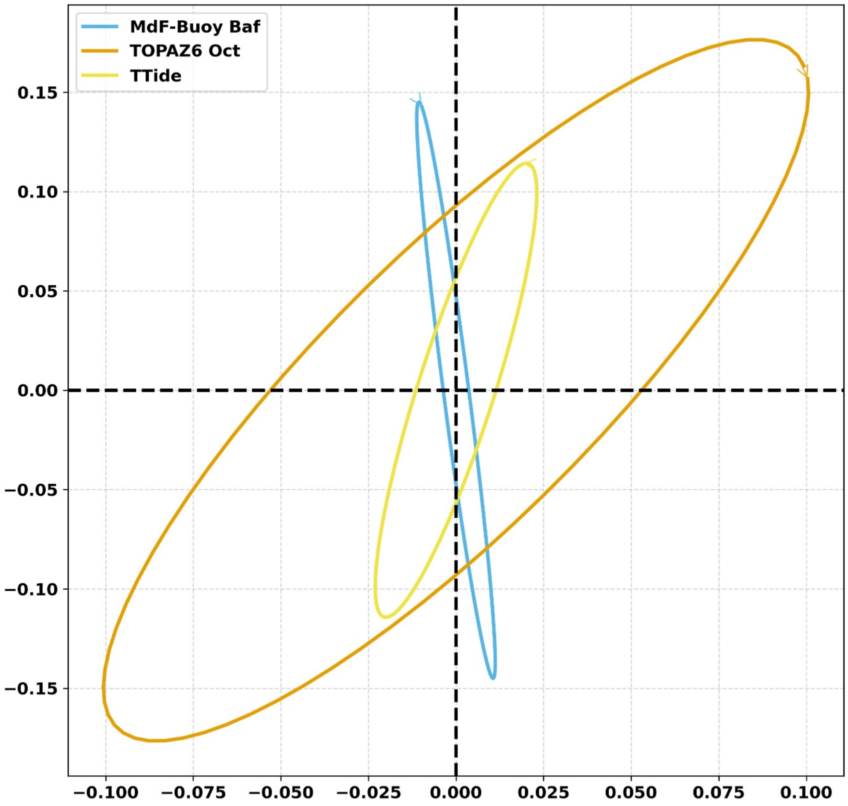

Figure 11. M_2 tidal ellipses from the MdF estimation on Buoy Baf (blue) and the underlying TOPAZ6 (green) value for the October 2018 period. The axes labels are in m/s.

models are unavailable. Additionally, our method assumes constant multiplicative factors in the estimation process (see Equation 13). This assumption could be a potential constraint in regions where it may not be applicable. To address this, one could either reduce the length of the trajectory or introduce variability in these factors. However, such modifications necessitate further research.

6. Summary and Conclusions

In this paper, we proposed a novel method to estimate the tidal current constituents from a single buoy trajectory addressing the limitations in the Arctic.

We show that traditional harmonic analysis applied to buoy velocities does not only suffer from the spatial variability of the tides, but the interaction between mean flow and tides may also introduce frequency shifts in buoy-observed amplitudes, challenging the efficacy of traditional tidal harmonic analysis. This phenomenon, similar to Doppler shift, was empirically investigated using buoy data from both barotropic and baroclinic dominant regions. We found that in barotropic dominant regions, such shifts are negligible due to the large tidal current wavelengths, typically around 1,000 km. In contrast, the shifts in the baroclinic dominant regions can be approximately computed by the Doppler shift formula.

Three case studies were conducted to assess the accuracy, robustness, and operational efficiency of our proposed method. In case 1 (Section 5.1), we demonstrated the method's accuracy and robustness through comparison with model results and noting the consistency of estimates derived from two different buoys. Case 2 (Section 5.2) involved a comparison with an independent moored observation in the barotropic dominant region of the Chukchi Sea, confirming the accuracy of the MdF method for estimating TCCs in such regions. In a baroclinic tidal region, the performance of the method is yet to be determined based on real control data. However, a simple synthetic experiment (case 3 Section 5.3) may be seen as an indication that the method can be applied in complex baroclinic environments.

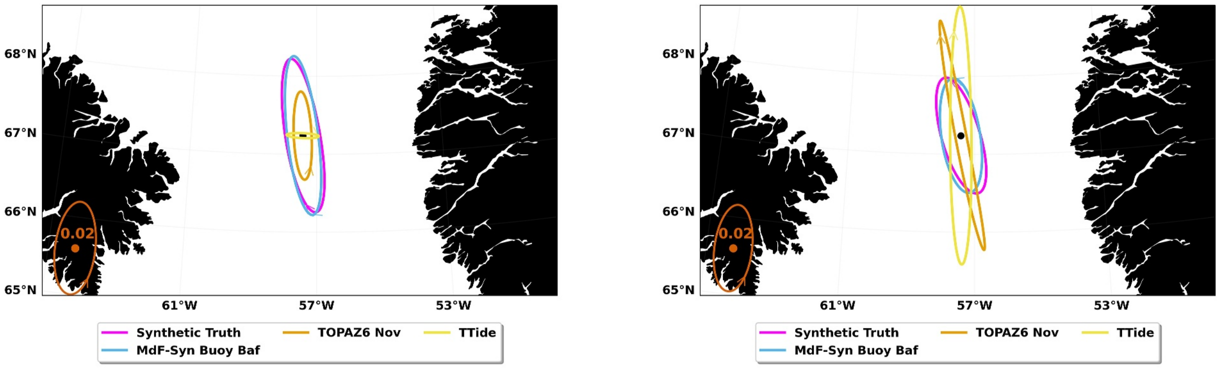

(a) M2

(b) S2

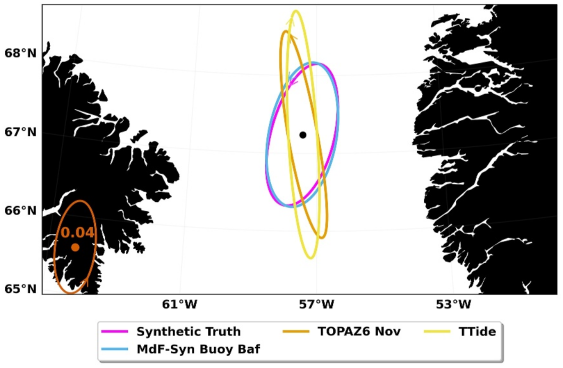

(c) K1

Figure 12. Tidal current ellipses for M_2, S_2 and K_1 constituents in the Baffin Bay region. The ellipse's center indicates the data set's location, arrows on the ellipse represent its rotation, while the ellipse's color denotes the data set type. The lower-left ellipse demonstrates the scale with the value at the center for the semi-major axis.

While TTide (Pawlowicz et al., 2002) remains a robust tool for harmonic analysis of stationary, long-term time series, our results highlight its limitations for short, moving buoy records in the Arctic. In particular, rapid spatial variations, Doppler-like frequency shifts, and inertial oscillations can cause standard tidal frequencies (e.g., M_2) to be misidentified or aliased to adjacent frequencies like S_2. These effects lead to larger amplitude and phase deviations, as evidenced by comparisons with moored ADCP observations. Consequently, TTide estimates may be unreliable in regions characterized by strong baroclinic tides or short buoy records.

In summary, our method has shown promising results when applied to buoys in various Arctic regions. It effectively incorporates spatio-temporal variations by utilizing model-based initial estimates. Additionally, the estimation of $2n$ parameters like in a standard tidal harmonic analysis coupled with a linearized estimation process makes it operationally efficient.

However, a more comprehensive validation of the MdF method, involving a wider range of buoys and independent observational data across both barotropic and baroclinic zones, is necessary to fully substantiate its applicability across the diverse Arctic regions. This is especially recommended in the case of baroclinic tidal regions with simultaneous measurement with buoys and ADCP.

Table 4
Vector Differences (VD_i) With Respect to the Ground Truth for the Meridional (v_t) and Zonal (u_t) Components

	u_t			v_t		
	TOPAZ6	Syn Buoy Baf	TTide	TOPAZ6	Syn Buoy Baf	TTide
M_2	0.030	**0.004**	0.09	0.077	**0.005**	0.09
S_2	0.022	**0.006**	0.034	0.028	**0.003**	0.037
K_1	0.027	**0.001**	0.015	0.016	**0.015**	0.033

Note. Values are compared from three sources: the TOPAZ6 initial estimates, the MdF-derived values for Syn Buoy Baf (obtained using TOPAZ6 initial estimates), and the corresponding TTide values. The best values are bold for legibility.

Furthermore, additional validation can be achieved by comparing the fixed amplitude ratios for S_2 and O_1 against M_2 and K_1 TCC respectively, between the model values and the buoy-derived estimates. Such validations are crucial for testing the assumptions, such as the constant multiplicative factor used in the MdF Method Equation 13. A representation of variable parameters with polynomials is one solution which can be investigated however, care should be taken that this might also lead to an illconditioned problem in the estimation similar to the methods from Lie et al. (2002) and others. Moreover, the reliance on good initial model estimates is a limitation when compared to existing approaches like those proposed by Lie et al. (2002) and Kodaira et al. (2016), although such models are becoming more readily available in recent years.

Appendix A: Results With FES2014b Model

A1. Case1: Barents Sea-Barotropic

Figure A1 shows the results at Case Study 1 locations obtained using FES2014b model output.

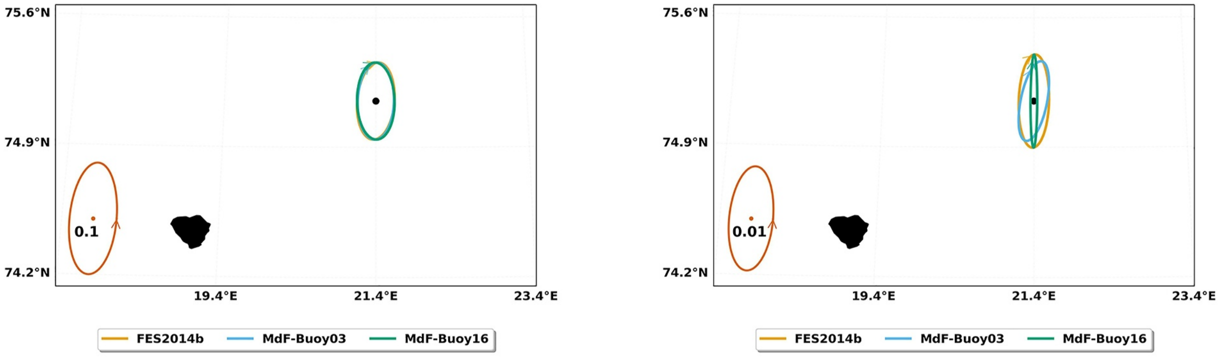

(a) M2

(b) S2

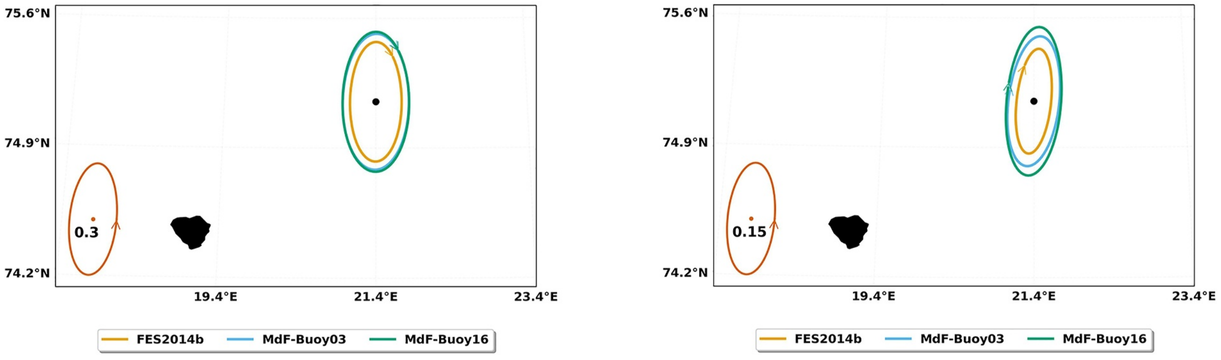

(c) O1

(d) K1

Figure A1. Tidal current ellipses for the 4 TCCs-M_2 (a), S_2 (b), O_1 (c), K_1 (d). The center of the ellipse indicates the comparison point (21.4°E, 75.15° N); arrows on the ellipse represent its rotation. The comparison is between FES2014b (orange), MdF applied to Buoy 03 (sky blue) and MdF applied to Buoy 16 (bluish green). The lower-left ellipse demonstrates the scale, with the magnitude of the semi-major axis given at the center in m/s.

A2. Case2: Chukchi Sea-Barotropic

Figure A2 shows the tidal ellipses with its corresponding values in Table A1 at Case Study 2 location obtained using FES2014b model output.

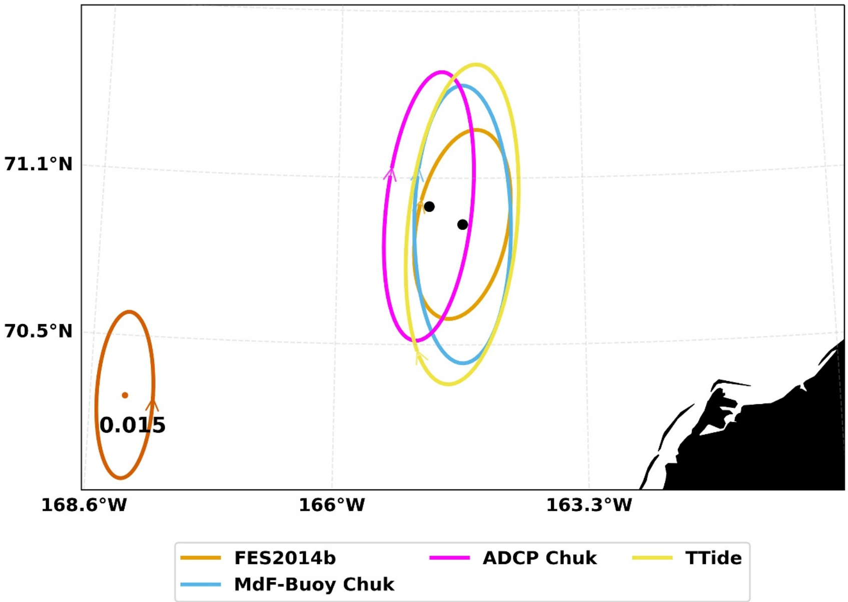

Figure A2. Tidal current ellipses for the M_2 constituent in the Chukchi Sea region. The ellipse's center indicates the data set's location, arrows on the ellipse represent its rotation, while the ellipse's color denotes the data set type. The lower-left ellipse demonstrates the scale, with its semi-major axis measuring 0.015 m/s.

Table A1.

Table A1
Comparison of the M_2 TCC Estimates at the ADCP Chuk Location

	u_t			v_t		
	H (m/s)	ϕ (deg)	VD (m/s)	H (m/s)	ϕ	VD (m/s)
ADCP Chuk	0.022	161.0	–	0.026	59.7	–
FES2014b	0.026	147.5	0.007	0.017	74.1	0.011
Buoy Chuk	**0.026**	**155.8**	**0.005**	**0.025**	**65.5**	**0.003**
TTide	0.031	217.1	0.026	0.028	141.4	0.036

Note. MdF method with FES2014b data is used for Buoy Chuk values and VD is with respect to ADCP data. H is for amplitude, ϕ is for phase. The best values are in bold for legibility.

Appendix B: Additional Results Case1: Barents Sea

Here we show the actual estimates of the 4 TCCs at the comparison point (21.4 °E, 75.15 °N) obtained from GTSM and the corresponding values of MdF method with GTSM applied to Buoy 03 and Buoy 16 (Table B1). Likewise, we also show the same values with FES2014b (Table B2).

Table B1
TCC Estimates at the Location (21.4°E, 75.15°N) Based on GTSM

	u_t						v_t					
	GTSM		Buoy 16		Buoy 03		GTSM		Buoy 16		Buoy 03	
	H	ϕ	H	ϕ	H	ϕ	H	ϕ	H	ϕ	H	ϕ
M_2	0.35	52.7	0.49	59.7	0.45	59.6	0.29	321.9	0.44	327.9	0.39	327.2
S_2	0.08	85.8	0.1	76.2	0.08	87.3	0.07	354.9	0.08	353.2	0.08	357.6
O_1	0.02	356.4	0.01	93.1	0.05	257.6	0.01	271.3	0.01	201.7	0.01	84.9
K_1	0.16	103.3	0.19	127.6	0.18	121.3	0.16	26.7	0.24	45.5	0.19	38.3

Note. The Buoy 03 and Buoy 16 values are derived using the MdF method applied to GTSM data. Amplitudes (H) are in m/s, and phase angles (ϕ) are in °.

Table B2
TCC Estimates at the Location (21.4°E, 75.15°N) Based on FES2014b

	u_t						v_t					
	FES2014b		Buoy 16		Buoy 03		FES2014b		Buoy 16		Buoy 03	
	H	ϕ	H	ϕ	H	ϕ	H	ϕ	H	ϕ	H	ϕ
M_2	0.34	46.9	0.44	45.2	0.44	46.8	0.32	317.6	0.38	315.5	0.37	318.3
S_2	0.08	86.1	0.08	98.1	0.08	107.9	0.07	3.4	0.07	6.2	0.07	20.9
O_1	0.01	95.2	0.002	113.9	0.01	99.7	0.01	10.0	0.01	28.2	0.01	37.5
K_1	0.11	119.1	0.18	153.6	0.17	152.2	0.14	45.2	0.2	74.7	0.18	76.2

Note. The Buoy 03 and Buoy 16 values are derived using the MdF method applied to FES2014b data. Amplitudes (H) are in m/s, and phase angles (ϕ) are in m/s.

Data Availability Statement

The study is carried out with data sets from Kaleschke and Müller (2022), IABP (2014), IABP (2018) and Baumann et al. (2020). The data generated and scripts used are available at Vasulkar (2025).

Acknowledgments
This work is part of the research programme FAST4NL with project number ALWPP.2017.001, which is (partly) financed by the Dutch Research Council (NWO). The Global Tide and Storm Surge (GTSM) software is developed on Delft3D Flexible Mesh Software which can be obtained from Deltares. This study has been conducted using E.U. Copernicus Marine Service Information; https://doi.org/10.48670/moi-00005.

References

Apel, J. R. (2003). A new analytical model for internal solitons in the ocean. *Journal of Physical Oceanography*, *33*(11), 2247–2269. https://doi.org/10.1175/1520-0485(2003)033⟨2247:ANAMFI⟩2.0.CO;2

Baumann, T. M., Polyakov, I. V., Padman, L., Danielson, S., Fer, I., Janout, M., et al. (2020). Arctic tidal current atlas. *Scientific Data 2020 7:1*, *7*(1), 1–11. https://doi.org/10.1038/s41597-020-00578-z

Bliss, A., Hutchings, J., Anderson, P., Anhaus, P., Belter, H. J., Berge, J., et al. (2022). Raw files for sea ice drift tracks from the Distributed Network of autonomous buoys deployed during the Multidisciplinary drifting Observatory for the Study of Arctic Climate (MOSAiC) expedition 2019–2021. *Arctic Data Center*. https://doi.org/10.18739/A2WW77163

Boylan, B. M. (2021). Increased maritime traffic in the Arctic: Implications for governance of Arctic sea routes. *Marine Policy*, *131*, 104566. https://doi.org/10.1016/J.MARPOL.2021.104566

Cancet, M., Andersen, O. B., Lyard, F., Cotton, D., & Benveniste, J. (2018). Arctide2017, a high-resolution regional tidal model in the Arctic Ocean. *Advances in Space Research*, *62*(6), 1324–1343. https://doi.org/10.1016/J.ASR.2018.01.007

Copernicus Marine Service. (2014). Global Ocean physics reanalysis. https://doi.org/10.48670/moi-00021

Erofeeva, S., & Egbert, G. (2018). Arc5km2018: Arctic ocean inverse tide model on a 5 kilometer grid. *urn:node:ARCTIC*. https://doi.org/10.18739/A21R6N14K

E.U. Copernicus Marine Service Information (CMEMS). (2018). Arctic Ocean tidal analysis and Forecast. *Marine Data Store (MDS)*. https://doi.org/10.48670/moi-00005

Fang, Y. C., Janout, M., Kawaguchi, Y., & Statscewich, H. (2022). Semidiurnal internal tides observed on the eastern Flank of Hanna Shoal in the Northeastern Chukchi Sea. *Journal of Geophysical Research: Oceans*, *127*(11), e2021JC018232. https://doi.org/10.1029/2021JC018232

Foreman, M. G., & Henry, R. F. (1989). The harmonic analysis of tidal model time series. *Advances in Water Resources*, *12*(3), 109–120. https://doi.org/10.1016/0309-1708(89)90017-1

GEBCO Bathymetric Compilation Group. (2019). The GEBCO_2019 Grid—a continuous terrain model of the global oceans and land (Tech. Rep.). *GEBCO British Oceanographic Data Centre, National Oceanographic Centre*.

Gill, A. (1982). Atmosphere-Ocean dynamics. *International Geophysics Series*, *30*.

Hasselmann, K. (1970). Wave-driven inertial oscillations. *Geophysical Fluid Dynamics*, *1*(3–4), 463–502. https://doi.org/10.1080/03091927009365783

IABP. (2014). LEVEL 1 data product. Retrieved from https://iabp.apl.uw.edu/Data_Products/BUOY_DATA/3HOURLY_DATA/

IABP. (2018). LEVEL 2 data product. Retrieved from https://iabp.apl.uw.edu/WebData/LEVEL2/

IABP. (2020). Deployment Plans. Retrieved from https://iabp.apl.uw.edu/overview_deploymentplans.html

Irazoqui Apecechea, M., Verlaan, M., Zijl, F., Le Coz, C., & Kernkamp, H. (2017). Effects of self-attraction and loading at a regional scale: A test case for the Northwest European Shelf. *Ocean Dynamics*, *67*(6), 729–749. https://doi.org/10.1007/s10236-017-1053-4

Kaleschke, L., & Müller, G. (2022). *Sea ice drift from autonomous measurements from 15 buoys, deployed during the IRO2/SMOSIce field campaign in the Barents Sea March 2014*. PANGAEA. https://doi.org/10.1594/PANGAEA.941334

Kodaira, T., Thompson, K. R., & Bernier, N. B. (2016). Prediction of M_2 tidal surface currents by a global baroclinic ocean model and evaluation using observed drifter trajectories. *Journal of Geophysical Research: Oceans*, *121*(8), 6159–6183. https://doi.org/10.1002/2015JC011549

Kodaira, T., Waseda, T., Nose, T., Sato, K., Inoue, J., Voermans, J., & Babanin, A. (2021). Observation of on-ice wind waves under grease ice in the western Arctic Ocean. *Polar Science*, *27*, 100567. https://doi.org/10.1016/J.POLAR.2020.100567

Koentopp, M., Eisen, O., Kottmeier, C., Padman, L., & Lemke, P. (2005). Influence of tides on sea ice in the Weddell Sea: Investigations with a high-resolution dynamic-thermodynamic sea ice model. *Journal of Geophysical Research*, *110*(C2), 1–12. https://doi.org/10.1029/2004JC002405

Lie, H.-J., Lee, S., & Cho, C.-H. (2002). Computation methods of major tidal currents from satellite-tracked drifter positions, with application to the Yellow and East China Seas. *Journal of Geophysical Research*, *107*(C1), 3. https://doi.org/10.1029/2001JC000898

Luneva, M. V., Aksenov, Y., Harle, J. D., & Holt, J. T. (2015). The effects of tides on the water mass mixing and sea ice in the Arctic Ocean. *Journal of Geophysical Research: Oceans*, *120*(10), 6669–6699. https://doi.org/10.1002/2014JC010310

Lyard, F. H., Allain, D. J., Cancet, M., Carrère, L., & Picot, N. (2021). FES2014 global ocean tide atlas: Design and performance. *Ocean Science*, *17*(3), 615–649. https://doi.org/10.5194/OS-17-615-2021

Müller, M., Cherniawsky, J. Y., Foreman, M. G., & Von Storch, J. S. (2014). Seasonal variation of the M_2 tide. *Ocean Dynamics*, *64*(2), 159–177. https://doi.org/10.1007/s10236-013-0679-0

Munchow, A., Coughran, C., Hendershott, M., & Winant, C. (1995). Performance and calibration of an acoustic Doppler current profiler towed below the surface. *Journal of Atmospheric and Oceanic Technology*, *12*(2), 435–444. https://doi.org/10.1175/1520-0426(1995)012<0435:pacoaa>2.0.co;2

Nyström, L. (2022). *Acoustic Doppler Current Profiling for streamflow measurements in subarctic climate*. Doctoral dissertation. Luleå University of Technology, Luleå. Retrieved from https://urn.kb.se/resolve?urn=urn:nbn:se:ltu:diva-92666

Pawlowicz, R., Beardsley, B., & Lentz, S. (2002). Classical tidal harmonic analysis including error estimates in MATLAB using T_TIDE. *Computers & Geosciences*, *28*(8), 929–937. https://doi.org/10.1016/S0098-3004(02)00013-4

Pease, C. H., Salo, S. A., & Overland, J. E. (1983). Drag measurements for first-year sea ice over a shallow sea. *Journal of Geophysical Research*, *88*(C5), 2853–2862. https://doi.org/10.1029/JC088iC05p02853

Poulain, P. M., & Centurioni, L. (2015). Direct measurements of World Ocean tidal currents with surface drifters. *Journal of Geophysical Research: Oceans*, *120*(10), 6986–7003. https://doi.org/10.1002/2015JC010818

Provost, C. L., Genco, M.-L., & Lyard, F. (1995). Modeling and predicting tides over the world ocean. In *Coastal and estuarine studies* (pp. 175–201). American Geophysical Union (AGU). https://doi.org/10.1029/CE047P0175

Raghukumar, K., Chang, G., Spada, F., Jones, C., Janssen, T., & Gans, A. (2019). Performance characteristics of "spotter," a newly developed real-time wave measurement buoy. *Journal of Atmospheric and Oceanic Technology*, *36*(6), 1127–1141. https://doi.org/10.1175/JTECH-D-18-0151.1

Simmons, H. L., Hallberg, R. W., & Arbic, B. K. (2004). Internal wave generation in a global baroclinic tide model. *Deep Sea Research Part II: Topical Studies in Oceanography*, *51*(25–26), 3043–3068. https://doi.org/10.1016/J.DSR2.2004.09.015

Vasulkar, A. (2025). Data and code accompanying deriving tidal constituent estimates from GNSS buoy data in the Arctic [Dataset]. *4TU. ResearchData*. https://doi.org/10.4121/11fda466-5008-47ec-99e5-19a9f9e1d431.v1

Vasulkar, A., Verlaan, M., Slobbe, C., & Kaleschke, L. (2022). Tidal dissipation from free drift sea ice in the Barents Sea assessed using GNSS beacon observations. *Ocean Dynamics*, *72*(8), 577–597. https://doi.org/10.1007/S10236-022-01516-W/FIGURES/14

Vasulkar, A., Verlaan, M., Slobbe, C., & Kulikov, M. (2024). Modelling the effect of sea ice in an ocean tide model. *Ocean Modelling*, *190*, 102405. https://doi.org/10.1016/J.OCEMOD.2024.102405

Veenstra, J. (2023). Hatyan: Tidal analysis and prediction. Retrieved from https://github.com/Deltares/hatyan

Verlaan, M., De Kleermaeker, S., & Buckman, L. (2015). GLOSSIS: Global storm surge forecasting and information system. In *Australasian coasts & ports conference 2015: 22nd Australasian coastal and ocean engineering conference and the 15th Australasian port and Harbour Conference* (pp. 229–234). Engineers Australia and IPENZ.

Wang, X., Verlaan, M., Apecechea, M. I., & Lin, H. X. (2021). Computation-efficient parameter estimation for a high-resolution global tide and surge model. *Journal of Geophysical Research: Oceans*, *126*(3), e2020JC016917. https://doi.org/10.1029/2020JC016917

Watkins, D. M., Bliss, A. C., Hutchings, J. K., & Wilhelmus, M. M. (2023). Evidence of Abrupt transitions between sea ice dynamical regimes in the East Greenland marginal ice zone. *Geophysical Research Letters*, *50*(15), e2023GL103558. https://doi.org/10.1029/2023GL103558

Wu, Y., Hannah, C., Petrie, B., Pettipas, R., Peterson, I., Prinsenberg, S., et al. (2013). Ocean current and sea ice statistics for Davis Strait (Tech. Rep.). *Darthmouth-Nova Scotia: Fisheries and Oceans Canada*.

Zhigang, X. (2002). Ellipse parameters conversion and velocity profiles for tidal currents in Matlab (Tech. Rep.). *Maurice Lamontagne Institute, Fishries and Oceans Canada*. https://doi.org/10.13140/RG.2.1.2515.4000